frontiers | Frontiers in Energy Research

ORIGINAL RESEARCH
published: 24 May 2022
doi: 10.3389/fenrg.2022.910842

Layered P2-$Na_xMn_{3/4}Ni_{1/4}O_2$ Cathode Materials For Sodium-Ion Batteries: Synthesis, Electrochemistry and Influence of Ambient Storage

*Lukas Fridolin Pfeiffer[1], Nicola Jobst[1], Cornelius Gauckler[1], Mika Lindén[2], Mario Marinaro[1], Stefano Passerini[3,4], Margret Wohlfahrt-Mehrens[1] and Peter Axmann[1]**

[1]Accumulators Materials Research (ECM), ZSW Center for Solar Energy and Hydrogen Research Baden-Württemberg, Stuttgart, Germany, [2]Institute for Inorganic Chemistry II, Ulm University, Ulm, Germany, [3]Helmholtz Institute Ulm, Ulm, Germany, [4]Karlsruhe Institute of Technology (KIT), Karlsruhe, Germany

Sodium-ion batteries promise efficient, affordable and sustainable electrical energy storage that avoids critical raw materials such as lithium, cobalt and copper. In this work, a manganese-based, cobalt-free, layered $Na_xMn_{3/4}Ni_{1/4}O_2$ cathode active material for sodium-ion batteries is developed. A synthesis phase diagram was developed by varying the sodium content *x* and the calcination temperature. The calcination process towards a phase pure P2-$Na_{2/3}Mn_{3/4}Ni_{1/4}O_2$ material was investigated in detail using *in-situ* XRD and TGA-DSC-MS. The resulting material was characterized with ICP-OES, XRD and SEM. A stacking fault model to account for anisotropic broadening of (10*l*) reflexes in XRD is presented and discussed with respect to the synthesis process. In electrochemical half-cells, P2-$Na_{2/3}Mn_{3/4}Ni_{1/4}O_2$ delivers an attractive initial specific discharge capacity beyond 200 mAh g^{-1}, when cycled between 4.3 and 1.5 V. The structural transformation during cycling was studied using *operando* XRD to gain deeper insights into the reaction mechanism. The influence of storage under humid conditions on the crystal structure, particle surface and electrochemistry was investigated using model experiments. Due to the broad scope of this work, raw material questions, fundamental investigations and industrially relevant production processes are addressed.

Keywords: electrochemistry 1, batteries 2, sodium 3, cathode 4, synthesis 5, ambient storage 6, layered oxide 7

OPEN ACCESS

Edited by:
Ivana Hasa,
University of Warwick,
United Kingdom

Reviewed by:
Qing Wang,
Northeastern University at Qinhuangdao, China
Liangtao Yang,
Shenzhen Institutes of Advanced Technology (CAS), China

****Correspondence:***
Peter Axmann
Peter.Axmann@zsw-bw.de

Specialty section:
This article was submitted to Electrochemical Energy Conversion and Storage, a section of the journal Frontiers in Energy Research

Received: *01 April 2022*
Accepted: *27 April 2022*
Published: *24 May 2022*

Citation:
Pfeiffer LF, Jobst N, Gauckler C, Lindén M, Marinaro M, Passerini S, Wohlfahrt-Mehrens M and Axmann P (2022) Layered P2-$Na_xMn_{3/4}Ni_{1/4}O_2$ Cathode Materials For Sodium-Ion Batteries: Synthesis, Electrochemistry and Influence of Ambient Storage. Front. Energy Res. 10:910842. doi: 10.3389/fenrg.2022.910842

1 INTRODUCTION

To combat man-made climate change, many societies are aiming to reduce their greenhouse gas emissions to net zero (UNFCCC, 2022). To reach this goal, electrical energy generation from renewable, green sources such as solar and wind is being quickly expanded (International Renewable Energy Agency, 2021). The intermittent nature of solar and wind requires great capacities of stationary electrical energy storage to stabilize the grid (Dunn et al., 2011). Additionally, the electrification of cars to reduce carbon dioxide emissions from internal combustion engines requires mobile electrical energy storage solutions. For both applications, electrochemical energy storage in batteries is one of the most promising technologies (Gür, 2018).

The continuous development of lithium-ion batteries (LIBs) since their first commercialization in 1991 by Sony has made LIBs today's most promising technology for electrochemical energy storage in mobile devices and grid scale applications (Armand et al., 2020). However, lithium-ion batteries

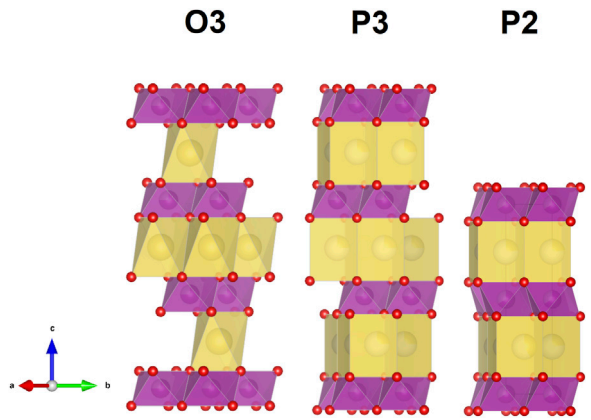

FIGURE 1 | Crystal structures obtained during synthesis of sodium layered transition metal oxides and their description in Delmas notation (O3, P3 and P2).

are incorporating critical raw materials in view of availability and economic importance, such as cobalt, lithium, copper and graphite (International Energy Agency, 2021). For the near future, the dependency of LIB production on these critical raw materials is expected to result in material shortages and increasing prices (Boer et al., 2021; Boer, 2022).

Sodium-ion batteries (SIBs) utilize a similar working principle as todays LIBs (Sun, 2020), but enable the replacement of the above-mentioned critical raw materials with highly abundant materials, such as sodium for lithium, hard carbon for graphite, and manganese-based, but cobalt-free oxides as host materials for positive (cathode) electrodes, which offer promising performance (Hasa et al., 2021; Tapia-Ruiz et al., 2021). Additionally, the copper current collector on the anode side can be replaced with the cheaper and lighter aluminum foil (Larcher and Tarascon, 2015; Vaalma et al., 2018; Tarascon, 2020). The similar production processes of LIBs and SIBs makes sodium-ion batteries a drop-in technology (Tarascon, 2020). The sum of these aspects is expected to result in reduced prices per energy storage capacity ($/kWh) for SIBs (Vaalma et al., 2018). Due to the higher potential of sodium compared to lithium and the higher ionic radius and mass of sodium ions versus lithium ions, SIBs most likely will not be able to exceed the energy density of the best LIBs (Tapia-Ruiz et al., 2021), but might offer advantages in terms of low temperature performance (Rudola et al., 2021), thermal stability (Kuze et al., 2013) and transportation/storage safety (Bauer et al., 2018). These aspects make SIBs a promising complementary technology to LIBs (Tarascon, 2020).

On the cathode side, layered sodium transition metal oxides and polyanionic compounds such as phosphates and Prussian blue analogues are currently considered in literature (Hasa et al., 2021). Among these materials, layered sodium transition metal oxides are considered among the most promising cathode active materials (CAMs) (Ortiz-Vitoriano et al., 2017; Goikolea et al., 2020; Gonzalo et al., 2021; Tapia-Ruiz et al., 2021) because of similar production processes and processability to LIB CAMs (Drop-In technology), high specific energy and fast solid Na^+ diffusion (Gonzalo et al., 2021). Following Delmas' classification for alkali metal layered oxides (Delmas et al., 1980), sodium transition metal oxides are denoted as either O3, P3 or P2 (see **Figure 1**). In this classification the alphabetic character specifies the alkali metal environment (here O for octahedral, P for prismatic) while the number refers to the MO_2 slabs in the hexagonal unit cell (here 3 or 2). Distorted phases are denoted with a prime (e.g., O'3, P'2). The oxygen stacking in O3-type materials follows an AB CA BC sequence. In P2-type materials, the oxygen stacking is AB BA (Delmas et al., 1980). Note that at room temperature metastable phases such as O2 are accessible *via* electrochemical (de) sodiation due to gliding of MO_2 slabs. Therefore, electrochemically induced transitions between O- and P-type structures can occur at room temperature (kinetic control). On the contrary, transitions between 2-type (e.g., P2) and 3-type (e.g., P3/O3) structures would require the breaking of metal oxygen bonds, which calls for elevated temperatures (synthesis conditions, thermodynamic control). Therefore, no electrochemically induced transitions between P2 and P3/O3 are possible at room temperature (Raphaël J. Clément et al., 2015). For intercalation type cathode materials such as layered alkali transition metal oxides (A_xMO_2), alkali metal ions (A) are reversibly (de)intercalated from/into the layered host structure, while charge neutrality is maintained by oxidation/reduction of the transition metal. The Fermi energy of the transition metal redox center is directly proportional to the potential of the cathode active material. Therefore, the operating potential of intercalation materials is highly influenced by the active transition metal redox center (Manthiram, 2017). Additionally, structural considerations (Padhi et al., 1997b) and inductive effects (Padhi et al., 1997a) can highly influence the Fermi energy and therefore the cathode potential.

O3-type sodium layered oxides typically undergo various phase transitions during electrochemical (de)sodiation (e.g., O3—O'3—P3—P'3) and exhibit slow insertion kinetics at a high degree of sodiation (Gupta et al., 2022). Additionally, these materials are often prone to poor stability in humid atmospheres (Wang et al., 2018; Sun, 2020). P2-type layered oxides on the other hand, typically operate within a broad solid solution range with high sodium-ion (de)insertion kinetics due to the wide diffusion channels of the prismatic sodium environments (Tarascon, 2020). Additionally, in O3-type structures such as nickel-rich NCM materials, a structural degradation from layered to spinel-type to rock salt structures is reported to be a common aging effect (Schipper et al., 2017; Bianchini et al., 2019). For lithium-ion exchanged P2-$Na_{2/3}Li_{1/6}Mn_{5/6}O_2$, Paulsen and Dahn reported stability against structural conversion to spinel, referring to its specific oxygen stacking sequence (J. M. Paulsen et al., 1999). For P2-type sodium layered oxides, a structural degradation pathway *via* the spinel structure therefore seems unlikely, due to the similarity of the oxygen stacking sequence. The main drawbacks of P2-type layered oxides is their sodium deficiency resulting in reduced full cell capacities (typically $x \sim 2/3$ in Na_xMO_2) (Tapia-Ruiz et al., 2021) and detrimental phase transitions at high degree of desodiation (e.g., P2—O2) (Kubota et al., 2018). In P2-type materials, phase transitions at high degree of desodiation can be mitigated by

doping (Gonzalo et al., 2021). Enhanced cycle stability was reported with doping of various elements such as Mg (Singh et al., 2016; Wang et al., 2016; Tapia-Ruiz et al., 2018), Al (Hasa et al., 2017), Ti (Yoshida et al., 2014; Bao et al., 2019), Fe (Hasa et al., 2014; Hasa et al., 2015; Feng et al., 2022), Co (Bao et al., 2017; Bao et al., 2018a; Bao et al., 2018b), Cu (Kubota et al., 2017; Zheng et al., 2017; Yang et al., 2021), Zn (Wu et al., 2016).

In literature, the most investigated P2-type materials are $Na_{2/3}CoO_2$, $Na_{2/3}MnO_2$ and $Na_{2/3}Ni_{1/3}Mn_{2/3}O_2$ (Tapia-Ruiz et al., 2021). Among these, P2-$Na_{2/3}Ni_{1/3}Mn_{2/3}O_2$ incorporates mainly uncritical and low-cost raw materials and offers promising electrochemical performance as cathode active material in sodium batteries. When cycled in sodium half-cells between 2.0—4.5 V, this material offers reversible discharge capacities beyond 160 mAh g^{-1} (Lu and Dahn, 2001a). Using *in-situ* XRD, Lu and Dahn observed a solid solution reaction between 2.0—4.0 V and a two-phase reaction at a voltage plateau of approximately 4.2 V. During charge up to 4.0 V within the P2 structure, the *a* lattice parameter decreased and the *c* lattice parameter increased. During the two phase reaction at approximately 4.2 V, a second phase, the O2-phase, with a smaller *c* lattice parameter emerged upon charge and the lattice parameters of the P2-phase remained constant. The authors suggested that the end members of the P2-O2 phase transition are P2-$Na_{1/3}Ni_{1/3}Mn_{2/3}O_2$ and O2-$Na_0Ni_{1/3}Mn_{2/3}O_2$ (Lu and Dahn, 2001a). During the P2-O2 phase transition, MO_2 slabs glide in the a-b plane in (*1/3 2/3 0*) or (*-1/3 -2/3 0*) direction (Kubota and Komaba, 2015), forming octahedral sodium vacancies between the MO_2 slabs. The random choice of gliding direction in the O2 structure causes stacking faults (Lu and Dahn, 2001a). The resulting oxygen stacking in the O2 phase follows the AB CB sequence (Lee et al., 2013). During desodiation of P2-$Na_xNi_{1/3}Mn_{2/3}O_2$, nickel is oxidized to compensate the charge between $2/3 > x > 1/3$. For the two phase region at $1/3 > x > 0$, anionic redox activity (oxidation of oxygen ions) was reported (Risthaus et al., 2019; Dai et al., 2020; Zhang et al., 2020). A *reductive coupling mechanism* between nickel and oxygen was proposed as charge compensation mechanism during the P2-O2 phase transition (Dai et al., 2020). At high degree of sodiation $x > 2/3$ the tetravalent manganese ions are partially reduced to compensate the charge (Risthaus et al., 2019). The voltage profile of P2-$Na_xNi_{1/3}Mn_{2/3}O_2$ exhibits distinct voltage jumps at $x = 2/3$, 1/2 and 1/3 (Lu and Dahn, 2001a). These voltage jumps were ascribed to sodium vacancy orderings within the alkali metal layers (Lee et al., 2013).

Increasing the manganese content to P2-$Na_{2/3}Mn_{3/4}Ni_{1/4}O_2$ results in a smoothed voltage profile (Manikandan et al., 2016; Gutierrez et al., 2018), which was related with a significant weakening of sodium/vacancy orderings within the alkali metal layer (Gutierrez et al., 2018). With respect to P2-$Na_xNi_{1/3}Mn_{2/3}O_2$, *in-situ* XRD on P2-$Na_xMn_{3/4}Ni_{1/4}O_2$ suggested a similar evolution of the crystal structure during electrochemical (de) sodiation at room temperature (Gutierrez et al., 2018). Additionally, a distorted P'2 phase was reported to form at the end of discharge (Gutierrez et al., 2018). To the best of our knowledge, no lattice parameters for the O2 structure have been reported so far for $Na_xMn_{3/4}Ni_{1/4}O_2$.

The specific crystal structure obtained during synthesis of sodium layered oxides depends on synthesis temperature, sodium content and transition metal composition (Paulsen and Dahn, 1999; Lei et al., 2014; Zhao et al., 2020; Xiao et al., 2021). In the $Na_{2/3}Mn_{1-y}Ni_yO_2$ system, Paulsen and Dahn investigated the influence of synthesis temperature and Mn/Ni ratio on the crystal structure. They reported P2 structures for high calcination temperatures (> 800°C) and low nickel contents $y \leq 1/3$. With decreasing nickel content, higher calcination temperatures are needed to form pure P2 structures (Paulsen and Dahn, 1999). Recently, Xiao et al. published the dependency of the crystal structure on the Mn/Ni ratio and sodium stoichiometry for a fixed calcination temperature of 900°C. Pure P2 structures evolve at nickel stoichiometries $y < 0.5$ and sodium contents $x > 0.67$ (Xiao et al., 2021). Access of sodium carbonate during synthesis was reported to enable the formation of the P2-structure at lower calcination temperatures, but can lead to Na_2CO_3 surface impurities (Sathiya et al., 2017).

When considering a rapid scale-up of sodium-ion batteries as a drop-in technology, the stability of sodium-ion cathode active materials in ambient atmospheres is of great interest (Kubota and Komaba, 2015). Lu and Dahn investigated the structural influence of water on P2-$Na_{2/3}Co_zNi_{1/3-z}Mn_{2/3}O_2$ (z = 0, 1/6, 1/3). For cobalt substituted samples, additional reflexes in the XRD pattern corresponding to co-intercalated water were reported. In contrast to cobalt substituted samples, no water co-intercalation was reported for P2-$Na_{2/3}Ni_{1/3}Mn_{2/3}O_2$ (Lu and Dahn, 2001b). By comparing various P2-type materials, Zuo et al. proposed a reaction mechanism for the P2-type materials in contact with different humid atmospheres: In humid, CO_2-free atmospheres, P2-type layered sodium oxides undergo a sodium/proton exchange with a formation of NaOH on the surface (analogous to nickel-rich NCM materials (Shkrob et al., 2017; Pritzl et al., 2019)). With low amounts of CO_2 in the atmosphere, the composition on the particle surface changes to Na_2CO_3. At high CO_2 concentrations in the atmosphere, $NaHCO_3$ was proposed as the resulting surface impurity (Zuo et al., 2020). These alkaline surface impurities were reported to result in defluorination of the PVdF binder and a subsequent agglomeration of the slurry, which is complicating the electrode production (Kubota and Komaba, 2015).

In this work, we present the synthesis and electrochemical characterization of a P2-$Na_xMn_{3/4}Ni_{1/4}O_2$ cathode active material with spherical morphology for sodium-ion batteries. The chosen synthesis route includes mixing of a spherical hydroxide precursor with NaOH followed by calcination. From various samples, a phase diagram for $Na_xMn_{3/4}Ni_{1/4}O_2$ cathode active materials for sodium-ion batteries was constructed. The calcination process of phase-pure P2-$Na_{2/3}Mn_{3/4}Ni_{1/4}O_2$ was investigated *in-situ* with XRD and TGA-MS in order to understand the synthesis process. X-ray diffraction patterns of resulting phase pure P2 materials exhibit anisotropic broadened (10*l*) peaks. A stacking fault refinement to account for this anisotropic broadening was performed and is discussed in respect to the synthesis path. The prepared phase pure P2-$Na_{2/3}Mn_{3/4}Ni_{1/4}O_2$ cathode active material provides electrochemically attractive capacities in

sodium half-cells. The change of the crystal structure during electrochemical (de)sodiation was investigated with *operando* XRD. The influence of storage in ambient air was investigated using model experiments under controlled humidity.

2 EXPERIMENTAL

2.1 Materials, Synthesis and Storage

A dense, spherical $Mn_{3/4}Ni_{1/4}(OH)_2$ precursor was prepared by co-precipitation under vigorous stirring in a continuous stirred tank reactor (CSTR, V = 1 L). Feed-in solutions were prepared from deaerated distilled water, $Mn(NO_3)_2 \cdot 4\ H_2O$ and $Ni(NO_3)_2 \cdot 6\ H_2O$ (Carl Roth), NaOH (Carl Roth) and NH_3 solution (Carl Roth). The reaction product was filtrated and washed to remove residual salt solution from the product and subsequently dried to obtain the $Mn_{3/4}Ni_{1/4}(OH)_2$ powder.

To construct the phase diagram in **Section 3.1**, varied amounts of NaOH (Carl Roth) were added as aqueous solution to the hydroxide precursor in a wet impregnation procedure. The wet impregnation process enables a homogenous distribution of the sodium source on the precursor and circumvents experimental uncertainties caused by the hydroscopic nature of NaOH. The dried, impregnated powder was calcined at 450°C in air for 5 h in a Nabertherm batch furnace and subsequently homogenized. Following, heat treatments in air at various temperatures (550–900 °C) were performed with the same Nabertherm batch furnace for 10 h. After calcination, the material was allowed to naturally cool down.

The selected material for a detailed physical and electrochemical characterization (**Section 3.2** and **Section 3.3**) was prepared as follows: The amount of sodium hydroxide added during the wet impregnation was adjusted to result in the ratio ϕ = Na/M = 0.68 to account for a slight loss of sodium during high temperature calcination. A pre-calcination at 350°C for 5 h in air was performed in a Nabertherm bath furnace. After homogenization, the material was calcined at 900°C for 10 h in air in the same furnace. The sample was allowed to cool down naturally to 200°C, at which point the material was directly transferred to a Büchi glass oven, where it was kept overnight at 200°C and dynamic vacuum ($<5 \cdot 10^{-2}$ hPa). Following, the dried powder was directly transferred into an Ar filled glovebox (MBraun, H_2O < 0.1 ppm, O_2 < 0.1 ppm). Electrode preparation and cell assembly was done in the same glovebox without any contact to the ambient.

For the model storage experiment (**Section 3.4**), portions of the same material batch were taken from the glovebox and stored over a saturated $Ca(NO_3)_2 \cdot 4\ H_2O$ (Sigma Aldrich) solution in a closed container. This closed container was placed in a temperature chamber set to 30°C. Both, humidity and temperature were continuously monitored with a Testo 184H1 USB data logger. After 1, 3, 7, and 14 days of storage, samples were taken and characterized with XRD, Raman, IR, SEM and electrochemical cycling in half-cell configuration.

2.2 Physical and Chemical Characterization

Chemical analysis of the powder samples was done by ICP-OES measurements (Spectro Arcos SOP) in a diluted aqua regia solution. Powder X-ray diffraction (XRD) was performed on a D8Advance (Bruker) in Bragg-Brentano geometry equipped with a Cu X-ray tube and a LynxeyeXE detector. Phase quantification of the prepared samples was performed *via* Rietveld Refinement with Topas V6 Software. Stacking Fault Refinement was carried out using Faults Software (Casas-Cabanas et al., 2016). For Faults software, the instrumental broadening of the utilized XRD setup was derived from measurements of silicon standard NIST640c. Capillary XRD measurements were performed for *ex-situ* investigation of desodiated electrodes to avoid any uptake of water (Kubota and Komaba, 2015). In an Ar filled glovebox, desodiated electrodes were recovered from CR2032 coin cells and thoroughly washed in DMC (Carl Roth). The electrode composite was removed from the aluminum current collector foil and filled in glass capillaries, which were sealed inside the glovebox. Capillary XRD measurements were performed on the same lab X-ray diffractometer (Bruker). Instrumental broadening was derived from measurements of NIST660c and NIST640c standards. Evaluation of the obtained patterns was performed using Rietveld Refinement in TOPAS V6 software. All structures in this publication were drawn with VESTA Software (Momma and Izumi, 2011). Non-ambient *in-situ* XRD was performed on a XPert-Pro diffractometer (Malvern Panalytical) with a Cu X-ray tube and a HTK-1200N non-ambient chamber (Anton Paar). The NaOH impregnated hydroxide precursor was heated in air to mimic the calcination process. The heating was performed at 5°C min^{-1} with 10 min hold time at the target temperature before the diffraction pattern was recorded. The applied temperature profile is presented with the diffraction data in **Section 3.1**. TGA-DSC-MS was used to gain further insights on the chemical reactions during the calcination process. A TGA-DSC (Netzsch STA 449C) coupled with a mass spectrometer (Netzsch QMS 403) was used for this purpose. The sample was placed in an Al_2O_3 crucible and heated at 10°C min^{-1} in a stream of air. To account for the influence of the crucible and air stream, the DSC measurement data was corrected using a blind measurement under the same conditions. The particle architecture and morphology was characterized with a Leo 1530 VP (Zeiss) scanning electron microscope (SEM). Images were generated with an Everhart-Thornley-SE-Detector and 5 kV acceleration voltage. The volume-based particle size distribution was determined with a Mastersizer Micro (Malvern Instruments) by laser diffraction. Raman spectra were collected using a 532 nm laser at a power of 2 W and a Rayleigh-filter on a confocal Raman microscope Senterra (Bruker). Attenuated total reflection Fourier transformed infrared spectroscopy (ATR-FTIR) was performed on an ALPHA Spectrometer (Bruker) with an ALPHA-P (Bruker) ATR unit. All NaMNO spectra were normalized with respect to their highest intensity. Na_2CO_3 (Sigma Aldrich), $NaHCO_3$ (Fluka) and NaOH (Sigma Aldrich) were used as reference materials.

2.3 Electrochemical Characterization

Electrodes were prepared by mixing the cathode active material, SuperP-Li (Timcal) and PVDF binder (Solvay Solef P5130) in a weight ratio of 84:8:8, respectively, dispersed in an adequate amount of N-Methyl-2-pyrrolidone (NMP, Sigma Aldrich). The homogenous slurry was casted using the doctor blade technique on aluminum foil (Korff). After drying, electrodes of 12 mm diameter were punched. For materials stored in ambient conditions (3d, 14d in **Section 3.4**),

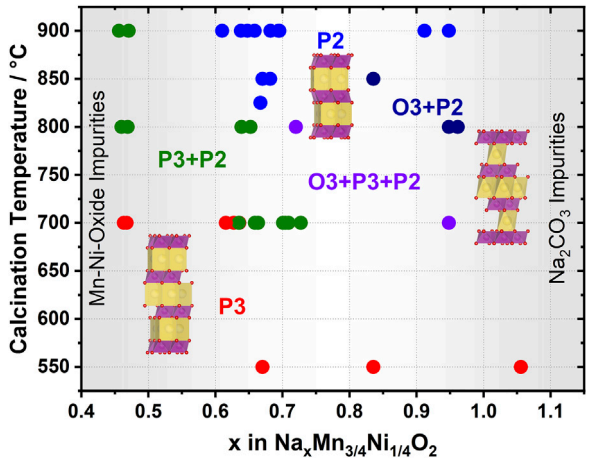

FIGURE 2 | Phase diagram obtained when varying the calcination temperature and the sodium content. The Mn/Ni ratio was kept constant by using the same $Mn_{3/4}Ni_{1/4}(OH)_2$ precursor. Refined crystal structures are visualized by red dots for P3, blue dots for P2, green dots for P3-P2, dark blue dots for O3-P2 mixtures and purple dots for mixtures of O3-P3-P2. The sodium content (*x*-axis) was derived from ICP-OES analysis, phase analysis was performed *via* Rietveld refinement of XRD patterns.

the electrode preparation was performed at the ambient. For all other materials, these processes were performed inside an Ar filled glovebox (MBraun, H_2O < 0.1 ppm, O_2 < 0.1 ppm) to avoid any influence of the ambient. Electrodes were dried in a Büchi glass oven at 130°C and dynamic vacuum (<$5 \cdot 10^{-2}$ hPa) overnight and directly transferred in the same Ar filled glovebox. CR2032 coin cells with an aluminum oxide protected positive pole (Hohsen) were prepared with the dried electrode, two layers of glass fiber separator (Whatman GFA), 150 µl 1M $NaPF_6$ (Fluorochem United Kingdom) in PC (BASF) electrolyte and a sodium metal (Acros Organics) counter electrode. The typical active material loading was ~4 mg cm^{-2}. A multichannel galvanostatic cell test system (CTS, Basytec) was used for the electrochemical cycling of the CR2032 coin cells. *Operando* XRD measurements were performed on a Stadi P (Stoe) diffractometer in transmission geometry. A curved Ge (111) crystal and a silver X-ray tube at 40 kV and 40 mA were utilized to obtain monochromatic $Ag_{K\alpha 1}$ (λ = 0.55941 Å) radiation. CR2032 coin cells were modified with polymer windows and were loaded with a cathode electrode (active material: SuperP: PVDF weight ratio 90:5:5; active material loading ~14 mg cm^{-2}), 150 µl electrolyte (1M $NaPF_6$ in PC + 5% FEC), two layers of glass fiber separator (GFA, Whatman) and a sodium metal counter electrode (Acros Organics). An Interface 1010E (Gamry) potentiostat was used for electrochemical cycling of the cells.

3 RESULTS AND DISCUSSION

3.1 Synthesis

A series of samples were prepared by mixing various amounts of NaOH as sodium source with a dense spherical $Mn_{3/4}Ni_{1/4}(OH)_2$ precursor and a subsequent calcination in air as described in the experimental section. The elemental composition of the obtained powders was analyzed using ICP-OES. From the ICP-OES results, a molecular formula following $Na_xMn_yNi_{1-y}O_2$ was calculated. Note, that the sodium content of the individual phases might differ, if two or more phases are present in one sample. The crystal structure of the powder samples was characterized by analysis of XRD patterns. The dependence of the obtained crystal structures on the calcination temperature and the sodium content is depicted in a color scheme in **Figure 2**.

At low temperatures (<700°C), exclusively the P3 layered structure type (red dots) was formed independent of the formal sodium content in the samples (0.45 < Na/M = *x* < 1.06). At medium temperatures (between 700 and 800°C), a mix of P3 and P2 layered structures (green dots) was identified for low sodium content *x* and a mix of P2 and O3 layered structures (dark blue dots) was detected for higher sodium content *x*. At high temperatures (≥ 825°C) and medium to high sodium contents (0.6 < *x* < 1.06) the material exhibits pure P2-type structure. At high sodium content sodium carbonate impurities are detected in the diffraction patterns (confirmed by ATR-FTIR spectroscopy, not shown here). At low sodium content *x*, sodium-free manganese-nickel-oxides are present besides the layered oxides (Ilmenite type $NiMnO_3$ below 700°C and Hausmannite-type Mn_3O_4 and $NiMn_2O_3$ above 800°C). The obtained crystal structure and impurities only depend on the calcination temperature and the sodium content *x*. No dependence of the hydroxide particle size was found (different sieving fractions: < 20 µm, 20–25 µm, 25–32 µm, 32–36 µm, > 36 µm). Therefore, we conclude, that the obtained structural composition is not influenced by the length of the transport pathways for sodium into the particles.

The obtained results are in good agreement with the literature for the same transition metal composition Mn/Ni = 3/1. With various sodium contents *x* > 0.6, Xiao et al. reported exclusively P2 phases to be present at a calcination temperature of 900°C (Xiao et al., 2021). Paulsen and Dahn predicted for a sodium content of *x* = 2/3, a phase transition from P3 to P2 phases to occur at approximately 830°C (Paulsen and Dahn, 1999). The results presented in **Figure 2** are in good agreement with both reported phase diagrams, and provide the additional, previously missing, information for a fixed transition metal ratio Mn/Ni = 3.

Due to the discussed advantages of P2-type materials, we selected phase pure P2-$Na_{2/3}Mn_{3/4}Ni_{1/4}O_2$ material for the following closer look on the synthesis process and in-depth characterization. To monitor the structural evolution during synthesis of a phase pure P2-type sodium manganese layered oxide, $Mn_{3/4}Ni_{1/4}(OH)_2$ precursor was mixed with NaOH solution to result in a sodium to metal ratio of Φ = Na/M = 2/3 and was calcined at different temperatures. At various stages, *ex-situ* powder XRD patterns were collected as presented in **Figure 3**. The XRD patterns of the pristine $Mn_{3/4}Ni_{1/4}(OH)_2$ precursor, the dried powder after impregnation with NaOH solution, the powder after calcination at 450°C in air and after 900°C in air show distinct differences from each other. Already wet impregnation with NaOH solution and drying resulted in a nearly complete transformation of the brucite-type structure of $Mn_{3/4}Ni_{1/4}(OH)_2$ precursor into a poorly crystalline P3-type structure. After calcination at 450°C in air, the transformation

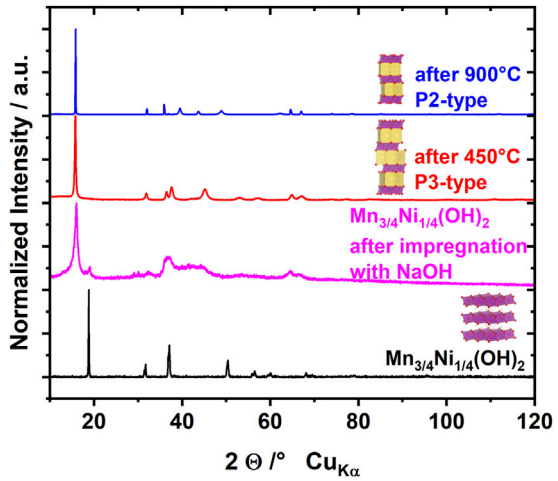

FIGURE 3 | *Ex-situ* powder XRD patterns of the fresh hydroxide precursor (black), the dry impregnated powder, the powder after calcination at 450°C in air and the phase pure P2 material after 900°C in air.

to P3 was complete. After calcination at 900°C a phase pure P2 material was obtained. For the $Mn_{3/4}Ni_{1/4}(OH)_2$ precursor, partial oxidation of the Mn^{2+} ions with ambient oxygen is reported in literature (Feitknecht et al., 1962; Owen, 1965; Ghosh, 2020), extracting v electrons per formula unit:

$$Mn_{3/4}Ni_{1/4}(OH)_2 + \frac{v}{4}O_2 \rightleftharpoons Mn_{3/4}Ni_{1/4}O_2H_{2-v} + \frac{v}{2}H_2O$$

After wet impregnation with NaOH solution and drying, the interlayer distance is enlarged compared to the pristine $Mn_{3/4}Ni_{1/4}(OH)_2$, which can be rationalized with the incorporation of sodium ions into the layered structure. Note, that the experimentally found interlayer distance differs from hydroxides, double layer hydroxides and Birnessites (Owen, 1965), but is in good agreement with P3-type sodium transition metal oxides. Based on this result, a partial exchange of the protons of the hydroxide precursor for sodium ions is proposed with insertion of u sodium ions per formula unit:

$$Mn_{3/4}Ni_{1/4}O_2H_{2-v} + \frac{2}{3}NaOH \rightleftharpoons Na_uMn_{3/4}Ni_{1/4}O_2H_{2-u-v} + \frac{u}{2}H_2O + \left(\frac{2}{3}-u\right)NaOH$$

To investigate the structural changes during calcination in more detail, *in-situ* XRD patterns are collected during the calcination process in air and presented in **Figure 4A**. Upon heating, the $(003)_{P3}$ reflex continuously shifts to lower 2Θ, indicating an increase of the interlayer distance and the c parameter of the P3 structure. Beyond 200°C the crystallinity of the P3 phase increases continuously till 800°C. In this temperature range, the a lattice parameter of the P3 structure is 2.91 Å, 2.89 Å and 2.92 Å and the c lattice parameter of the P3 structure is 17.01 Å, 17.06 Å and 17.05 Å at 250, 450 and 800°C, respectively. Between 825 and 875°C the structure transforms from P3 to P2. No changes were observed for the crystal structure during the 3 hour holding time at 900°C. The P2 structure exhibits lattice parameters of a = 2.93 Å and c = 11.30 Å. During cool down, no further changes were observed in the diffraction pattern except for a thermally induced shrinkage of the unit cell. Rietveld refinements of the obtained diffraction patterns were performed and the obtained information is presented in **Figure 4B**. Note, that all $(10l)_{P2}$ reflexes appear broadened, which will be discussed in the following section. A waterfall diagram of the diffraction patterns is provided in the supporting information **Supplementary Figure S1**.

To gain further insight into the structural transformation process, the chemical reactions during the calcination process were investigated with *in-situ* TGA-DSC-MS as presented in **Figure 5**. In the TGA-DSC-MS experiment, a first weight loss can be observed between 80—150°C, which is accompanied by an endothermal reaction and the formation of water (m/z = 18). With a reaction onset of 210°C, a second endothermal signal is observed in the DSC measurement. This reaction leads to the formation of water and carbon dioxide (m/z = 44). Whereas the evolution of water is peaking at a temperature of 300°C and is not observed beyond 420°C (m/z = 18 on baseline level), carbon dioxide is evolving till 900°C. Total mass loss after reaching 900°C accounts for 7%.

Below 200°C, *in-situ* XRD measurements revealed a shift towards higher interlayer distances of the P3 structure, which could be caused by further sodiation of the P3 structure. In the same temperature range, the TGA-DSC-MS measurement showed an endothermic reaction and a loss of water vapor. The endothermic response is expected for evaporation of water. Therefore, analysis of XRD and TGA-DSC-MS data suggests that residual NaOH may act as a sodium source for further sodiation of a partially sodiated P3 phase with additional w sodium ions per formula unit:

$$Na_uMn_{3/4}Ni_{1/4}O_2H_{2-u-v} + \left(\frac{2}{3}-u\right)NaOH \rightleftharpoons Na_{u+w}Mn_{3/4}Ni_{1/4}O_2H_{2-u-v-w} + \frac{w}{2}H_2O + \left(\frac{2}{3}-u-w\right)NaOH$$

From 200 to 450°C, the *in-situ* XRD experiment showed an increase of crystallinity of the P3 phase, a shrinkage of the a lattice parameter and increase of the interlayer distance (c lattice parameter) of the P3 structure. The *operando* TGA-DSC-MS experiment showed evolution of H_2O and CO_2 from 200 to 450°C. As no carbonates have been used for synthesis, CO_2 most likely originates from Na_2CO_3 formed from the reaction of NaOH and CO_2 from ambient air during impregnation and drying:

$$2\,NaOH + CO_2 \rightleftharpoons Na_2CO_3 + H_2O$$
$$NaOH + CO_2 \rightleftharpoons NaHCO_3$$
$$2\,NaHCO_3 \rightleftharpoons Na_2CO_3 + CO_2 + H_2O$$

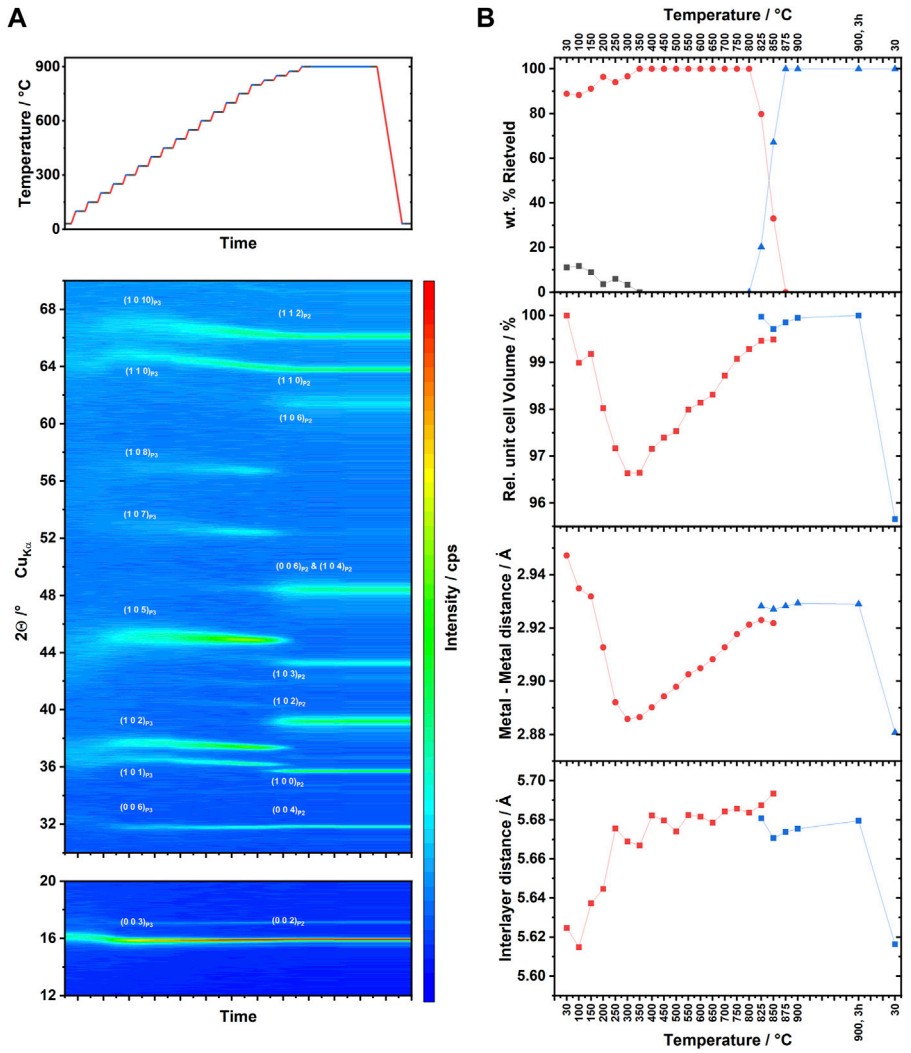

FIGURE 4 | *In-situ* XRD calcination of $Na_{2/3}Mn_{3/4}Ni_{1/4}O_2$ in air. **(A)** The temperature profile is represented in the upper diagram. The obtained diffraction pattern is represented as a heat map in the lower diagrams. **(B)** Refined weight fractions, change of the unit cell volume, metal-metal distance (*a* lattice parameter) and interlayer distance (proportional to *c* lattice parameter).

In fact, Na_2CO_3 and $NaHCO_3$ is detected with ATR-FTIR on the dried hydroxide precursor after impregnation with NaOH and on the powder after calcination at 450°C in air (**Supplementary Figure S2**). The evolution of water vapour and carbon dioxide (200–450°C) in the TGA-DSC-MS measurement and the increasing interlayer distance in the *in-situ* XRD experiment, can be rationalized by further sodiation of the layered structure, with NaOH, $NaHCO_3$ or Na_2CO_3 as sodium source adding x sodium ions per formula unit:

$$Na_{u+w}Mn_{3/4}Ni_{1/4}O_2H_{2-u-v-w} + \left(\frac{2}{3}-u-w\right)NaOH \rightleftharpoons Na_{u+w+x}Mn_{3/4}Ni_{1/4}O_2H_{2-u-v-w-x} + \frac{x}{2}H_2O + \left(\frac{2}{3}-u-w-x\right)NaOH$$

The shrinkage of the *a* lattice parameter (metal-metal distance) in **Figure 4B**, suggests an ongoing oxidation of the transition metals within this temperature range.

$$Na_{u+w+x}Mn_{3/4}Ni_{1/4}O_2H_{2-u-v-w} + \frac{2-u-v-w-x}{4}O_2 \rightleftharpoons Na_{u+w+x}Mn_{3/4}Ni_{1/4}O_2 + \frac{2-u-v-w-x}{2}H_2O$$

From 450 to 800°C, *in-situ* XRD showed a further increase in crystallinity of the P3 structure, an increasing *a* lattice parameter and a constant *c* lattice parameter. In the TGA-DSC-MS experiment, solely CO_2 evolved above 450°C. These results suggest a further sodiation of the structure with Na_2CO_3 as sodium source. Note, that a further sodiation of the structure

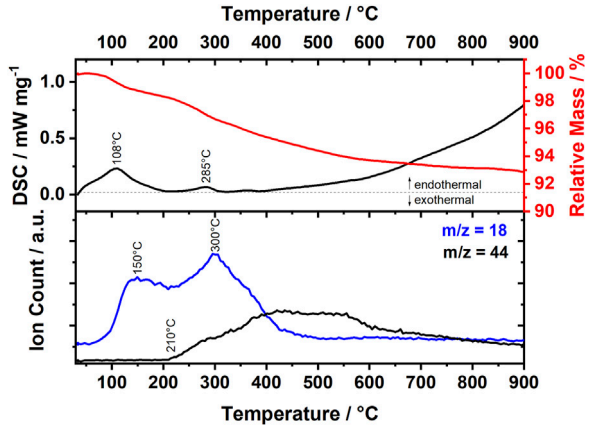

FIGURE 5 | *Operando* TGA-DSC-MS calcination in air.

requires a reduction of the transition metals, which is in accordance with the increasing *a* lattice parameter.

$$Na_{u+w+x}Mn_{3/4}Ni_{1/4}O_2 + \frac{2/3-u-w-x}{2}Na_2CO_3 \rightleftharpoons Na_{2/3}Mn_{3/4}Ni_{1/4}O_2 + \frac{2/3-u-w-x}{2}CO_2 + \frac{2/3-u-w-x}{4}O_2$$

From 825 to 875°C, *in-situ* XRD showed the structural transition from P3 to P2. In the same temperature range, no significant weight loss and no DSC response occurred in the TGA-DSC-MS, indicating a pure structural transformation in absence of chemical reactions. Note that the observed weight loss of 7% is below the expected weight loss of approximately 11% for the overall reaction:

$$Mn_{3/4}Ni_{1/4}(OH)_2 + \frac{2}{3}NaOH + \frac{1}{3}O_2 \rightleftharpoons Na_{2/3}Mn_{3/4}Ni_{1/4}O_2 + \frac{4}{3}H_2O$$

This experimentally observed discrepancy between the experiment and the theoretical weight loss further supports a partial sodium/proton exchange after wet impregnation and drying of the hydroxide precursor with NaOH solution.

3.2 Physical Characterization

A phase pure P2 material was prepared from the same hydroxide precursor and in similar fashion as the materials reported in the previous section. A detailed description of the material preparation can be found in the experimental section. In this section a detailed physical characterization of the material is presented. Electrochemical characterization as well as a model storage experiment based on the same material is presented in the following sections.

The chemical composition of the material as determined with ICP-OES is $Na_{0.64}Mn_{0.74}Ni_{0.26}O_2$. Powder X-ray diffraction pattern of this material is presented in **Figure 6**. All reflexes of the diffraction pattern can be assigned to ICDD PDF 01-070-3726 and described with space group $P6_3/mmc$ (194) with lattice parameters a = 2.883 Å and c = 11.184 Å. Additionally, (10*l*) peaks are significantly broadened. Such anisotropic broadening was ascribed to stacking faults in the literature and "O3- or P3-type" stacking faults were proposed to account for anisotropic broadening of (10*l*) peaks (Yabuuchi et al., 2012). To the best of our knowledge, no refinement of the actual structural stacking fault model has been reported so far.

In the ideal P2 structure, the stacking of the transition metals follows a CC arrangement (metals stacked on top of each other) and oxygen is stacked in AB BA sequence (Delmas et al., 1980). By introducing a stacking fault with a (*2/3 1/3 1/2*) transition vector, the stacking sequence of the transition metal is transformed to CA resulting in broadening of the (10*l*) peaks (see **Figure 6**). In this specific layer, sodium exhibits a prismatic environment with shared edges and faces with the transition metal octahedra such as in P3-type structures (oxygen stacking AB BC CA). Note, that other stacking faults can account for a similar anisotropic broadening, but would result in octahedral environment of the sodium ions. Since octahedral environments usually result in smaller *c* lattice parameters and hence additional reflexes in the diffraction pattern, these stacking faults have been ruled out.

As reported above, the material maintains a P3 structure during calcination up to 800°C. Between 825 and 875°C the structure transforms from P3 to P2. This structural transformation requires a breakage and reassembly of all the transition metal oxygen bonds of every second MO_2 slab. Using structural visualization with polyhedra, the P3 to P2 transformation can be described as a 60° rotation of all metal oxygen octahedra of every second MO_2 slab. The transformation from P3 to P2 most likely starts at random points within one crystallite and proceeds from these points until the growing P2 domains meet. If the oxygen stacking of the meeting P2 domains does not fit to the ideal AB BA oxygen stacking of the P2 structure, stacking faults remain. The refined stacking fault probability of 11.6% suggests an average number of nine MO_2 slabs per P2 domain.

For our material no notable change of the diffraction pattern did occur even after additional 40 h at 900°C (not shown here), which indicates that the stacking faults remain stable. From an energetic point of view, this could be rationalized, as the elimination of these stacking faults would require the breakage of all transition metal oxygen bonds of one of the neighboring P2 domains, which comes with a high energy barrier.

The particle morphology and architecture was characterized with SEM. The obtained images are presented in **Figures 7A–B**. The material consist of spherical, dense particles with micrometer sized crystals. A particle size distribution of this material is presented in **Figure 7C**. The powder offers a narrow particle size distribution (D_{10} = 7.7 µm, D_{50} = 13.2 µm, D_{90} = 21.1 µm), well suited for large scale slurry and electrode processing. Due to the chosen synthesis route, the material can easily be scaled up. In fact, the production of 350 g of this material was successful.

3.3 Electrochemical Characterization

After calcination, the material was processed without any further contact with the ambient. Electrochemical characterization of CR2032 coin cells in half-cell configuration is presented in **Figure 8**. The cells were cycled at C/10 (17.3 mA g^{-1}) for the

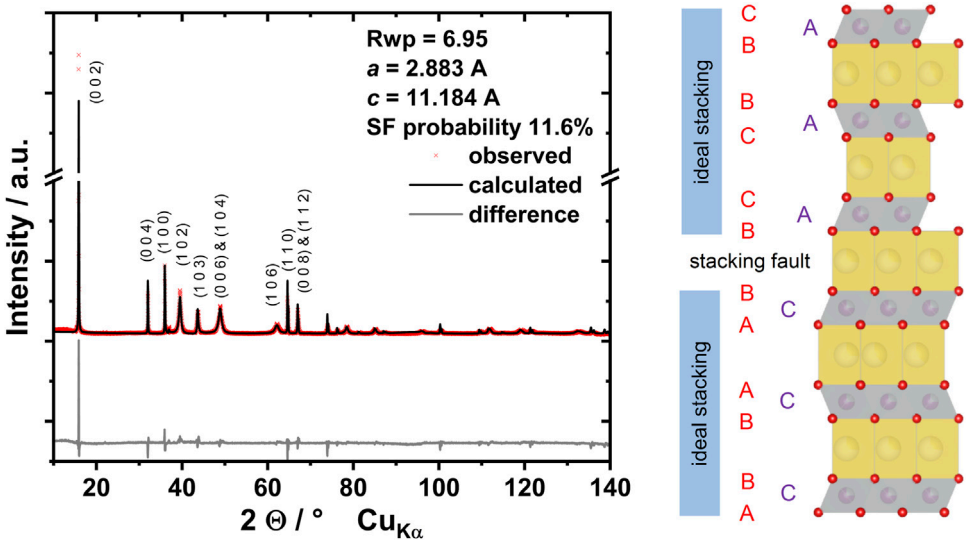

FIGURE 6 | Refined powder XRD pattern of a phase pure P2 material with stacking faults (left) and schematic representation of the stacking fault sequence (right).

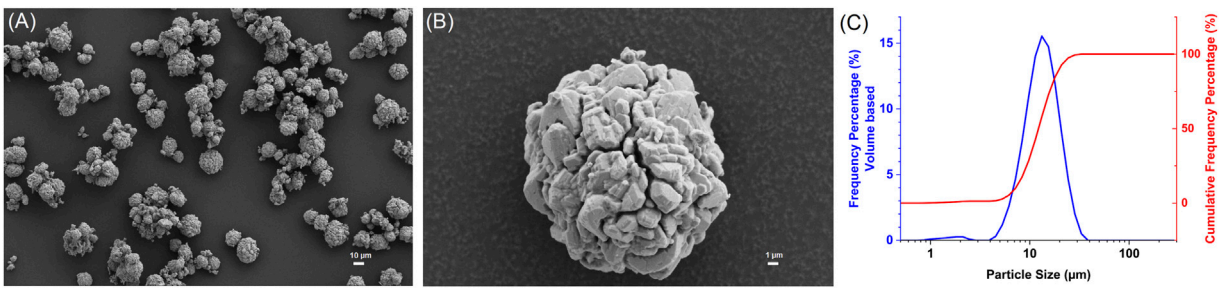

FIGURE 7 | SEM images at **(A)** low and **(B)** higher magnification. **(C)** particle size distribution of P2- $Na_{0.64}Mn_{3/4}Ni_{1/4}O_2$ material.

first three cycles, followed by C/3 (57.8 mA g^{-1}) in the subsequent cycles. Every tenth cycle, a check-up cycle at C/10 (17.3 mA g^{-1}) was performed. For the initial discharge and the subsequent first cycle, the sodium content of the active material was calculated based on the active material specific charge. The voltage profile is presented in **Figure 8A**. During the initial sodiation (discharge) to 1.5 V, the material is sodiated to x = 0.87. During the desodiation a plateau at approximately 2.0 V arises. Further desodiation results in a smooth voltage profile till a sodium stoichiometry of x = 1/3 is reached, at which point the cell voltage sharply rises from 3.9 to 4.2 V. Further desodiation results in a voltage plateau, indicating a two phase reaction. At a sodium content of x = 0.07, the cell voltage reaches the upper cut off at 4.3 V. During the subsequent re-sodiation, the cell voltage mimics the desodiation process with small hysteresis until $x \approx$ 0.65. Further galvanostatic sodiation exhibits increased hysteresis between sodiation and desodiation cell voltage. At the end of cycle 1, the calculated sodium stoichiometry is x = 0.84 at 1.5 V, indicating some irreversible losses during the first cycle. At sodium stoichiometries of x = 2/3 and x = 1/2, slight shoulders in the voltage profile are evident. For the same sodium contents, sodium vacancy orderings were reported in the closely related material P2-$Na_xNi_{1/3}Mn_{2/3}O_2$ (Lee et al., 2013). Therefore, shoulders of the voltage profile in **Figures 8A,B**, might be related to sodium/vacancy ordering. A deeper investigation on sodium/vacancy ordering in P2-$Na_xMn_{3/4}Ni_{1/4}O_2$ is currently in preparation. In **Figure 8B**, selected charge and discharge curves are presented. During the first cycle, attractive specific discharge capacities of approximately 202 mAh g^{-1} are reached. These initially high specific discharge capacities fade upon cycling. In cycle 10 and 30, the discharge capacities are 165 mAh g^{-1} and 161 mAh g^{-1}, respectively. The capacity fade is mainly caused by a progressive capacity loss on the high voltage plateau, combined with a progressive shift to lower discharge potentials. The voltage curves between 1.5 and 4.0 V maintain their original shape. The cycle stability is presented in **Figure 8C**. The specific discharge capacity fades considerably during the first three cycles at C/10. During the subsequent cycles at C/3 and C/10, it stabilizes with a linear capacity fade at a much lower rate. The couloumbic efficiency of the first three cycles averages to 97.5%

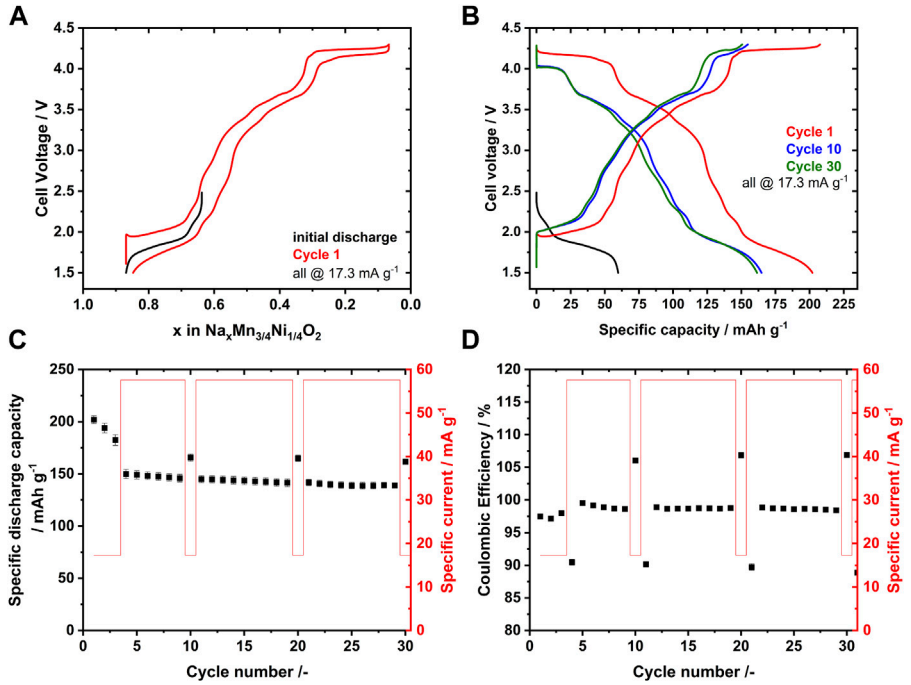

FIGURE 8 | Electrochemical characterization of phase pure P2-$Na_{0.64}Mn_{3/4}Ni_{1/4}O_2$ in sodium half-cells. **(A)** potential profile of initial discharge and cycle 1 **(B)** charge and discharge potentials of cycle 1, cycle 10 and cycle 30 **(C)** specific discharge capacity of the first 30 cycles **(D)** coulombic efficiency of the first 30 cycles. In **(C,D)** points represent an average value of three cycles. The standard deviation of these cells is presented as error bars. Cycles 1, 2, 3, 10, 20, 30 are performed at 17.3 mA g^{-1} (C/10), all other cycles are performed at 57.8 mA g^{-1} (C/3).

(**Figure 8D**). During the cycling at C/3, the average coulombic efficiency is 99.1%. The deviation from the average coulombic efficiency in cycle 4, 10, 11, 20, 21 and 30 are caused by the cycling protocol: the change of the specific current density between cycles causes the jumps of the coulombic efficiency. Prolonged cycling for 110 cycles with the same cycling protocol is presented in **Supplementary Figure S3** of the supporting information. After 100 cycles 50% of the initial capacity remains. The origin of the capacity fade will be addressed in detail in an upcoming publication. In literature similar voltage profiles and comparable specific capacities were reported (Manikandan et al., 2016; Gutierrez et al., 2018). Several reasons for capacity fade were reported for P2-$Na_xMn_{1-y}Ni_yO_2$ materials such as cracking due to anisotropic volume change (Yoshida et al., 2014; Kubota et al., 2017), exfoliation (Liu et al., 2016; Alvarado et al., 2017) and partial irreversibility of oxygen redox (Dai et al., 2020; Zhang et al., 2020).

Operando XRD was performed for the initial sodiation and the first full cycle to gain further insights into the sodium storage mechanism and the evolution of the crystal structure during sodium (de)intercalation. The obtained voltage profiles during the initial discharge (light blue), the first charge (red) and first complete discharge (blue) are presented with the associated diffraction patterns as a heat map in **Figure 9** (left). The full diffraction patterns are presented in the supporting information **Supplementary Figure S4** as a waterfall diagram. The voltage profile of this *operando* setup closely matches the voltage profile obtained from regular coin cells as presented in **Figure 8**. During the initial discharge, the (002) and (004) peaks shifted to higher diffraction angles, indicating a decrease of the *c* parameter. Subsequent charge to 4.0 V, lead to a shift in opposite direction, indicating an increase of the *c* parameter. At the 4.2 V voltage plateau, the positions of the (002) and (004) peaks remained constant and the intensity decreased. At the end of charge, an additional broad peak at $2\Theta \approx 7^{\circ}$ (d ≈ 4.6 Å) emerged, which can be assigned to $(002)_{O2}$ peak of the O2 structure (Lu and Dahn, 2001a). In the subsequent discharge, the $(002)_{O2}$ peak disappeared and the (002) and (004) peaks of the P2 structure increased in intensity during the course of the voltage plateau. Through further discharge the (002) and (004) peaks shifted to higher angles, pointing to an increase of the *c* parameter.

The (100), (102), (103) and (110) peaks shifted to lower angles during the initial discharge, indicating an increase of the *a* parameter. Through the subsequent charge, these peaks shifted towards higher angles, pointing to a contraction of the *a* parameter. In the course of the voltage plateau at 4.2 V, the *a* parameter of the P2 structure remained constant. No additional peaks arising from the O2 structure can be clearly detected from the *operando* XRD, most likely due to severe broadening of the peaks caused by natural occurrence of stacking faults in the O2 structure (Lu and Dahn, 2001a). From our *operando* XRD data, no indication for a Jahn-Teller distorted P'2 structure (orthorhombic or monoclinic) (Gutierrez et al., 2018) can be derived.

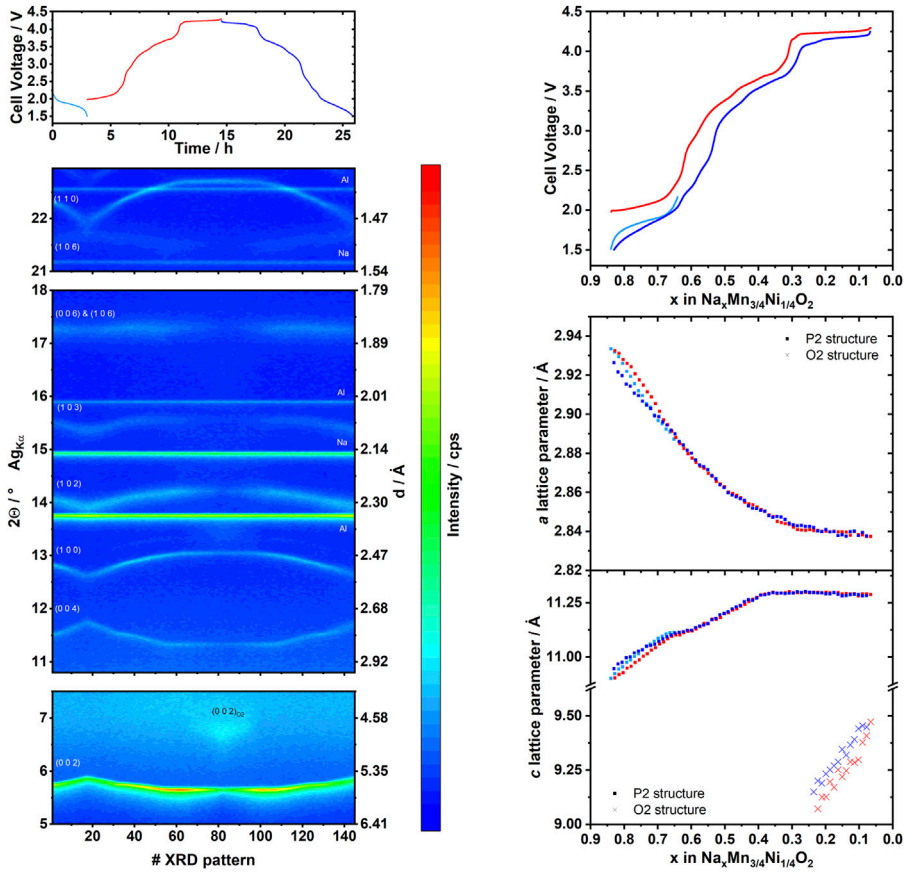

FIGURE 9 | *Operando* XRD: (left) measured cell voltage during the *operando* XRD and heat map of the obtained diffraction patterns. (right) cell voltage for the calculated sodium stoichiometry and refined lattice parameters.

Figure 9 (right) shows the correlation between cell voltage and refined lattice parameters with the calculated sodium content as *x*-axis. For each sodium stoichiometry, the lattice parameters are in good agreement and independent from the applied current direction, indicating structural reversibility. With decreasing sodium content, the *a* lattice parameter shows a nearly linear decrease between $0.84 < x < 0.35$ and remains constant at sodium stoichiometries $x < 0.35$. The *c* lattice parameter of the P2 phase shows a continuous increase with decreasing sodium content between $0.84 < x < 0.35$ and remains constant at sodium stoichiometries $x < 0.35$. Refined values of the *c* lattice parameter of the O2 phase emerging at the end of charge, are significantly smaller than the *c* lattice parameters of the P2 phase. A significant mechanical stress on the crystallites is expected due to this lattice collapse (Yoshida et al., 2014; Kubota and Komaba, 2015). Our refinements result in a linear increase of the *c* lattice parameters of the O2 structure during desodiation.

A solid solution of the sodium ions within the layered host structure is strongly suggested in the voltage window of 1.5–4.0 V, as phase analysis clearly shows a single phase (P2) with gradually changing lattice parameters and a smooth voltage profile in the electrochemical measurement (Robert A. Huggins, 2009). Within the solid solution regime, the course of the *a* lattice parameter can be rationalized with the radii of the active metal ions, which are reversibly oxidized during desodiation to compensate the charge (Mn^{3+} ~ 0.65 Å, Mn^{4+} ~ 0.53 Å, Ni^{2+} ~ 0.69 Å, $Ni^{3+}_{(LS)}$ ~ 0.56 Å, Ni^{4+} ~ 0.48 Å) (Kubota et al., 2018). The characteristic change of the *c* lattice parameter within the solid solution regime can be rationalized with sodium ions shielding the repulsive forces of oxygen ions of neighboring MO_2 slabs. During sodiation, additional sodium ions are intercalated into the structure, increasing the positive charge stored between the oxygen ions and therefore shielding the repulsion in between neighboring MO_2 slabs. As a result, the interlayer distance (d = *c*/2) decreases during sodiation (discharge). During desodiation (charge), sodium ions are removed from the structure, resulting in increasing repulsive forces between the oxygen ions and an increase of the interlayer distance. In the course of the 4.2 V voltage plateau, two phases with constant lattice parameters and inverse course of intensity are simultaneously detected (P2 and O2), proving a two-phase reaction at the 4.2 V voltage plateau. For the O2 phase, the increasing *c* lattice parameters during desodiation are unanticipated. For a pure two-phase reaction, constant lattice parameters are to be expected (Robert A. Huggins, 2009). The change of the *c* lattice parameter of the O2 structure, might originate from a narrow solubility range of

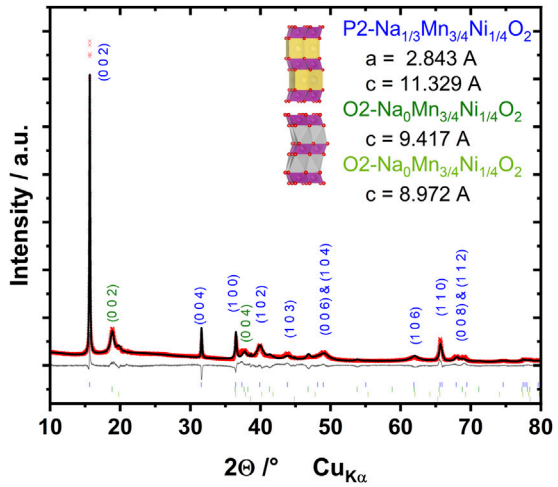

FIGURE 10 | Refinement of *ex-situ* XRD pattern of desodiated electrode at x = 1/6 obtained in capillary transmission. Measured data as red crosses, refined pattern as black line, difference as grey line.

sodium in the O2 structure or a *reductive coupling mechanism* between nickel and oxygen as proposed for $Na_xNi_{1/3}Mn_{2/3}O_2$ at low degree of sodiation (Dai et al., 2020). Overall, our *operando* XRD results are in good accordance with previous reports (Manikandan et al., 2016; Gutierrez et al., 2018). Based on literature and stoichiometric considerations, the formal active redox couples are Mn^{3+}/Mn^{4+} for $x < 1/2$, Ni^{2+}/Ni^{3+} for $1/2 < x < 1/3$ and $Ni^{3+}/Ni^{3+\delta}$ or O^{2-}/O^{n-} ($n = 2-\delta$) for $x < 1/3$ (Bao et al., 2017; Risthaus et al., 2019; Dai et al., 2020; Zhang et al., 2020).

Ex-situ characterization to gain further insights into the crystal structure of the O2 phase was performed. The obtained diffraction pattern for an electrode charged to a formal sodium stoichiometry of x = 1/6 is presented in **Figure 10**. In the obtained diffraction pattern, the sharpest peaks can be assigned to the P2 structure. Different from *operando* measurement, two O2 phases were detected. Both O2 phases differ in *c* lattice parameter. In the refinement, the following four structure models were included: a P2 structure with a sodium content of x = 1/3 (approximate onset of the two-phase reaction), an O2 structure with a *c* lattice parameter of 9.417 Å, a second O2 structure with a smaller *c* lattice parameter of 8.972 Å and aluminum (originating from the current collector foil). The *c* lattice parameter of the two O2 structures correspond to the endpoints of the range obtained from *operando* XRD. The (002) and (004) peaks of both O2 structures are clearly evident, while all other peaks are severely broadened. In contrast, only one O2 structure with an intermediate *c* lattice parameter was detected at the same sodium stoichiometry in the *operando* XRD. In the *operando* XRD the cell is under galvanostatic cycling conditions and therefore a certain kinetic control must be considered. For the *ex-situ* measurement a thermodynamic equilibrium can be assumed. The difference might arise from a certain solubility range of sodium in the O2 structure or a *reductive coupling mechanism* between nickel and oxygen as reported for $Na_xNi_{1/3}Mn_{2/3}O_2$ (Dai et al., 2020). To gain a full picture, further investigations on the processes occurring at the 4.2 V voltage plateau in $Na_xMn_{3/4}Ni_{1/4}O_2$ are required.

3.4 Effect of Storage

To evaluate the stability of our spherical P2-$Na_{0.64}Mn_{3/4}Ni_{1/4}O_2$ material in ambient atmospheres, a model storage experiment was performed. A schematic illustration of the experimental setup is presented in **Figure 11A**. The material was stored at controlled temperature in a closed container over a saturated $Ca(NO_3)_2$ solution. The *deliquescence relative humidity* (DRH) of $Ca(NO_3)_2 \cdot 4\ H_2O$ at 30°C was reported to be 46.7% (Adams and Merz, 1929; Guo et al., 2019). Using a humidity and temperature tracker, we monitored the storage conditions. The average temperature was 27.6°C and the relative humidity was 48.3% with high accuracy over the course of the 14 days storage experiment. Samples are taken after 1, 3, 7 and 14 days of storage.

To check the bulk stability over the course of the model storage experiment, powder X-ray diffraction was performed. The obtained diffraction patterns are presented in **Figure 11B**. No additional peaks are evident from the diffraction patterns, indicating a structural stability under applied conditions. Refined lattice parameters and stacking faults are reported in **Table 1**. No significant change of the *a* lattice parameter and the stacking fault probability is observed, but the *c* lattice parameter decreases during the storage experiment. The change in *c* lattice parameter can be rationalized with a sodium/proton exchange and the formation of amorphous surface NaOH, $NaHCO_3$ or Na_2CO_3 due to the reaction with absorbed water and the ambient atmosphere (Zuo et al., 2020). To obtain further information on the local structure, confocal Raman spectroscopy was performed on the stored materials and representative spectra are presented in **Figure 11C**. The bands with Raman shifts between 200 cm^{-1} and 700 cm^{-1} can be assigned to A_{1g}, E_{1g} and E_{2g} modes of the P2-type material (Iliev et al., 2004). To the best of our knowledge, so far the band assignments for P2-type sodium transition metal layered oxides in literature are not consistent (Iliev et al., 2004; Lemmens et al., 2004; Qu et al., 2006; Yang et al., 2006; Singh et al., 2015; Wang et al., 2016). From the obtained Raman spectra, no change of the local crystal structure is evident over the course of the model storage experiment. For all stored materials, sharp Raman bands around 1080 cm^{-1} corresponding to the υ_1 symmetric stretching vibration of the carbonate group in Na_2CO_3 (Buzgar and Ionut Apopei, 2009) were evident in certain local areas, while in other areas no sodium carbonate bands could be detected. This suggests locally formed sodium carbonate impurities on the particles. ATR-FTIR was performed to allow a semi-quantitative comparison. With ATR-FTIR many particles are simultaneously probed, providing statistically averaged spectra. The obtained spectra of stored materials with reference materials are presented in **Figures 11D,E**. Sodium carbonate is the dominant surface species for all stored materials. The intensity of the Na_2CO_3 bands clearly increases with storage time.

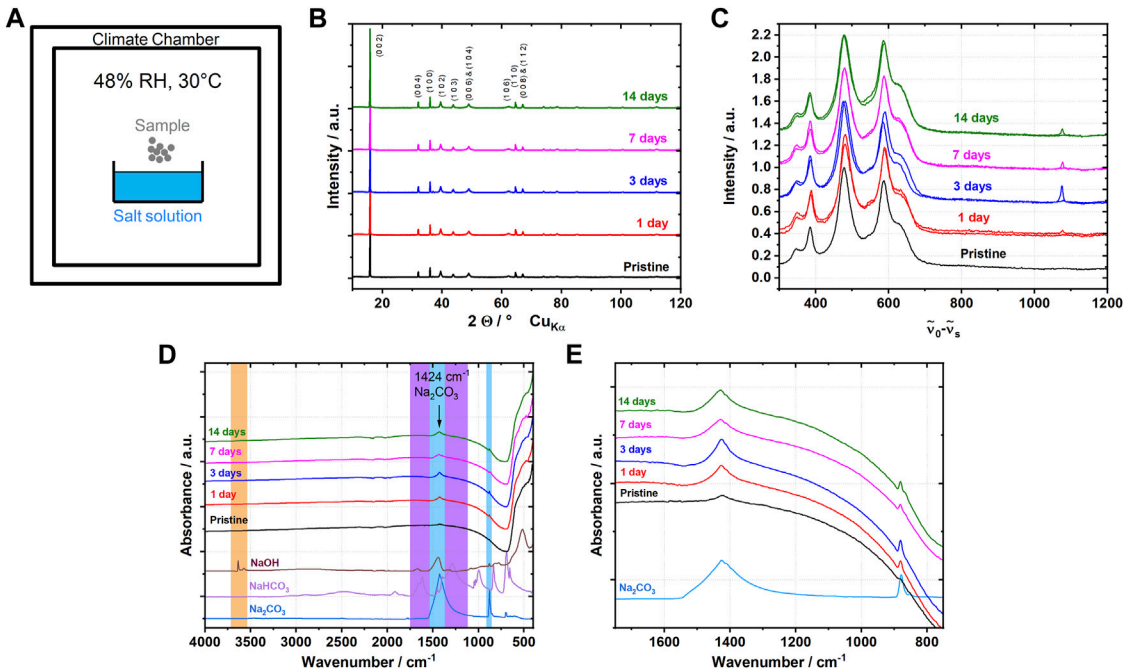

FIGURE 11 | (A) Schematic representation of model storage experiment, **(B)** XRD patterns of pristine and stored materials, **(C)** representative Raman spectra of pristine and stored materials, **(D)** ATR-FTIR spectra of pristine, stored and reference materials and **(E)** zoom-in into ATR-FTIR spectra.

TABLE 1 | Lattice parameters and stacking fault probabilities derived from refinement of X-ray diffraction patterns of pristine and stored materials.

	Lattice parameter		SF probability/%
	a/Å	*c*/Å	
14 days	2.882	11.168	12.0
7 days	2.881	11.168	12.1
3 days	2.883	11.176	12.2
1 day	2.881	11.177	12.2
Pristine	2.883	11.184	11.6

SEM images of the pristine, 3 days stored and 14 days stored material are shown in **Figure 12**. As presented above, the pristine material exhibited a clean surface with micrometre sized crystals. After 3 days of storage, the surface of the material was covered with a surface film and small dots appeared on the surface. After 14 days of storage, the surface of the material resembled the pristine one, but needle like structures were attached to the spherical particles. Such needle like structures on sodium layered oxides were previously reported for materials stored in humid air (Duffort et al., 2015; Zuo et al., 2020). Based on EDX and XRD, these needles are reported to consist of $NaHCO_3$ or Na_2CO_3 type compounds (Duffort et al., 2015; Zuo et al., 2020).

Characterization results on a similar material (P2-$Na_{0.69}Mn_{3/4}Ni_{1/4}O_2$) stored at higher relative humidity in a similar setup (60–68% RH, approx. 30°C) are presented in the supporting information **Supplementary Figure S5**. The bulk structure remains intact and no water co-intercalation is observed in XRD patterns (**Supplementary Figure S5A**) independent of the high relative humidity. No change of the local structure is apparent from Raman spectra (**Supplementary Figure S5B**). The

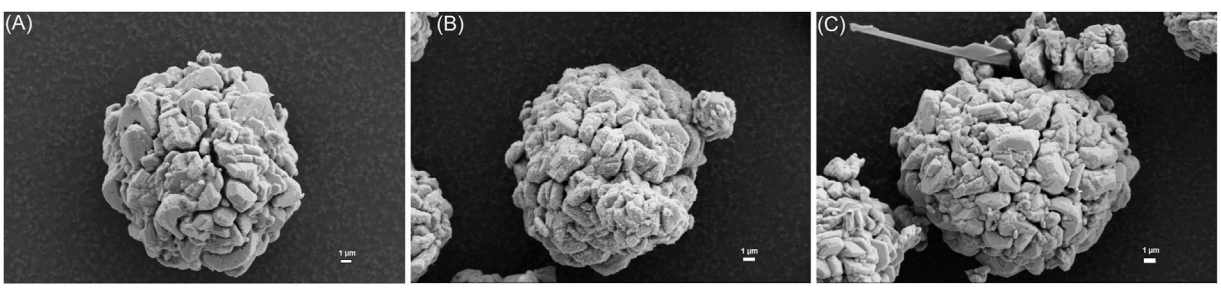

FIGURE 12 | SEM images of **(A)** pristine, **(B)** 3 days stored material and **(C)** 14 days stored material.

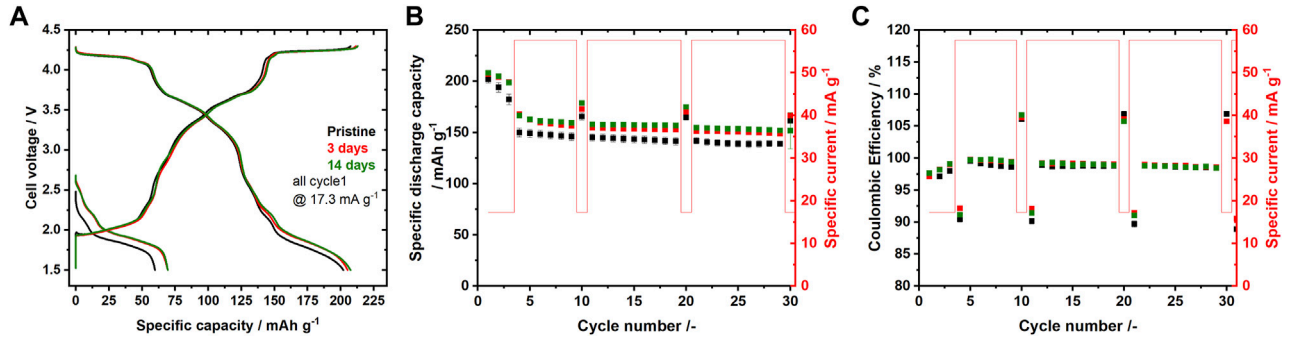

FIGURE 13 | (A) charge and discharge potential profiles of cells with pristine, 3 and 14 days stored material, **(B)** corresponding specific discharge capacity for the first 30 cycles and **(C)** coulombic efficiency of the first 30 cycles. For **(B,C)** every point represents an average of three cells, the standard deviation is presented as error bars.

dominant surface species is Na_2CO_3 as determined with ATR-FTIR (**Supplementary Figures S5C,D**). The amount of adsorbed water is determined with Karl-Fischer titration (**Supplementary Figure S5E**). Up to 0.45 %wt. of water is absorbed during the first days of storage. With prolonged storage, the amount of absorbed water decreases slightly and the amount of surface Na_2CO_3 increases. Overall, results obtained during storage at 60–68% relative humidity (**Supplementary Figure S5**) agree well with the above-described results at 48% RH (**Figure 11**).

Our results strongly suggest the uptake of water with subsequent sodium/proton exchange and the formation of Na_2CO_3 on the particle surface as a result of humid ambient storage. These results are in good accordance with the proposed reaction mechanism in literature (Zuo et al., 2020). The formed surface films were not uniformly distributed on the particle surface. Upon prolonged storage, needle like sodium carbonate compounds formed on the particle surface.

To evaluate the influence of storage on the electrochemical performance of the material, coin cells were prepared from the material stored for 3 and 14 days. The electrochemical results of these cells are compared with the pristine material in **Figure 13**. Voltage curves for the initial sodiation and the first cycle are presented in **Figure 13A**. The OCV of the pristine, 3 days stored and 14 days stored material was 2.48, 2.68 and 2.69 V, respectively. Higher charge uptake during the initial galvanostatic sodiation was observed for the stored materials compared to the pristine material. For the first cycle, the voltage profiles of all three materials are very similar. The cycling stability is presented in **Figure 13B**. During the first cycle all three materials offered similar specific discharge capacities. In the subsequent cycles, both stored materials exhibited slightly less capacity fading, resulting in higher discharge capacities for the stored material. The coulombic efficiency, as presented in **Figure 13C**, is very similar for all three materials.

Overall, the electrochemical cycling of the materials in coin cells seems not affected by the prolonged storage in humid ambient conditions. But the increased OCV and the higher capacity during the initial discharge, indicates a loss of active sodium due to storage. In a full cell with an initially sodium-free anode, a loss of active sodium directly translates into reduced capacity and reduced energy density of the full cells. Additionally, a negative effect of the formed alkaline surface films on the processability in PVdF based slurries is anticipated (Kubota and Komaba, 2015) and a more pronounced gassing in full cells can be expected as reported for lithium-ion batteries (Zhang, 2014; Jung et al., 2018; Sicklinger et al., 2019; Teichert et al., 2020). From a process point of view dry room conditions could be used to avoid the reaction with humid atmosphere, however this is associated with higher cost for the processing. From a materials point of view, a stabilisation *via* compositional variation (Zuo et al., 2020) or application of protective surface coatings allow direct processing of sodium ion cathode materials in standard large scale production.

4 CONCLUSION

In this work, we report a study on the synthesis, electrochemistry and ambient storage of $Na_xMn_{3/4}Ni_{1/4}O_2$ layered oxides as cathode materials in sodium-ion batteries. Analogue to large scale production of layered oxides for LIBs, spherical dense particles were manufactured *via* co-precipitation of a hydroxide precursor which subsequently was calcined with various amounts of sodium hydroxide at a number of temperatures.

By structural analysis of a series of samples, a phase diagram was constructed. The obtained phase diagram is in good agreement with previous reported results (Paulsen and Dahn, 1999; Xiao et al., 2021) and provides the previously missing information for Mn/Ni = 3. At intermediate sodium content and high calcination temperature, phase pure P2 materials form.

Further investigations on the synthesis process of P2-$Na_{0.64}Mn_{3/4}Ni_{1/4}O_2$ were performed by *ex-situ* XRD, non-ambient *in-situ* XRD and TGA-DSC-MS:

(i) After wet impregnation and drying in ambient conditions, the material exhibits a mixture of the hydroxide precursor and a poorly crystalline P3 structure.
(ii) From room temperature to 450°C, a sodiation and crystallization of the P3 structure together with a

complete oxidative removal of protons from the material is proposed.

(iii) From 450 to 800°C, further sodiation of the P3 structure together with a reduction of the transition metals is proposed.

(iv) Between 800 and 875°C, the structure is transformed from P3 to P2.

The obtained P2 material exhibits anisotropic broadening of the (10*l*) reflexes. A stacking fault model incorporating P3-type sodium sites was proposed. These stacking faults most likely remain between neighbouring P2 domains, during the structural transformation from P3 to P2.

The material reached an attractive initial specific discharge capacity of 202 mAh g^{-1} in electrochemical half-cells at specific currents of 17.3 mA g^{-1}. A capacity fade associated with the 4.2 V voltage plateau occurred, which will be discussed in an upcoming publication. In accordance with literature, we found a solid solution regime (P2 structure) between 1.5 and 4.0 V ($0.86 > x > 1/3$) and a two-phase reaction (P2—O2) at the 4.2 V voltage plateau.

The stability of the material during prolonged ambient storage was investigated. Even after 14 days of storage, no hydrated phases were detected. In accordance with literature (Zuo et al., 2020), we found Na_2CO_3 on the particle surfaces of stored materials. No effect of these sodium carbonate surface impurities was found on the electrochemical cycling in half-cells.

With this publication, we provide fundamental insights into the synthesis of $Na_xMn_{3/4}Ni_{1/4}O_2$ layered oxides. The developed synthesis route is analogous to the highly scalable production process of NCM materials and leads to sodium cathode materials with technically relevant particle specifications. The obtained phase pure P2 materials, are solely based on low-cost and abundant raw materials, offer promising electrochemical performance and a high storage stability in ambient atmospheres.

DATA AVAILABILITY STATEMENT

The raw data supporting the conclusions of this article will be made available by the authors, without undue reservation.

AUTHOR CONTRIBUTIONS

LP synthesized the sodium containing materials, conducted most of the physical characterization and the electrochemical characterization, performed data analysis and drafted and edited the manuscript. NJ performed the TGA-DSC-MS measurements and assisted with evaluation of the obtained data. CG and MM performed the operando XRD measurement. ML provided the possibility for non-ambient XRD and contributed with his knowledge and many discussion to the quality of this manuscript. MM, SP, and MW-M provided guidance for materials and electrochemistry and contributed with their knowledge to the quality of this manuscript. PA supervised the work and co-edited this manuscript.

FUNDING

This work was funded by the German Federal Ministry of Education and Research (BMBF) in the projects TRANSITION (03XP0186C), ExcellBattMat (03XP0257A and 03XP0257C) and the German Research Foundation (DFG) in the project POLIS Cluster of Excellence (ProjectID 390874152).

ACKNOWLEDGMENTS

The authors thank Samuel Blessing for the non-ambient *in-situ* XRD measurement, Wolfgang Weirather for his work on the hydroxide precipitation, Gisela Arnold for ICP-OES measurements, Adam Reupert for the introduction to the *operando* XRD setup, Premsyl Beran for help with the refinement of XRD instrument parameters, Gemma Maskell for language editing and all colleagues for many productive discussions.

SUPPLEMENTARY MATERIAL

The Supplementary Material for this article can be found online at: https://www.frontiersin.org/articles/10.3389/fenrg.2022.910842/full#supplementary-material

REFERENCES

Adams, J. R., and Merz, A. R. (1929). Hygroscopicity of Fertilizer Materials and Mixtures. *Ind. Eng. Chem.* 21, 305–307. doi:10.1021/ie50232a003

Alvarado, J., Ma, C., Wang, S., Nguyen, K., Kodur, M., and Meng, Y. S. (2017). Improvement of the Cathode Electrolyte Interphase on P2-Na2/3Ni1/3Mn2/3O2 by Atomic Layer Deposition. *ACS Appl. Mat. Interfaces* 9, 26518–26530. doi:10.1021/acsami.7b05326

Armand, M., Axmann, P., Bresser, D., Copley, M., Edström, K., Ekberg, C., et al. (2020). Lithium-ion Batteries - Current State of the Art and Anticipated Developments. *J. Power Sources* 479, 228708. doi:10.1016/j.jpowsour.2020.228708

Bao, S., Luo, S.-h., Wang, Z.-Y., Yan, S.-X., and Wang, Q. (2019). Improving the Electrochemical Performance of Layered Cathode Oxide for Sodium-Ion Batteries by Optimizing the Titanium Content. *J. Colloid Interface Sci.* 544, 164–171. doi:10.1016/j.jcis.2019.02.094

Bao, S., Luo, S.-h., Wang, Z.-Y., Yan, S.-X., Wang, Q., and Li, J.-y. (2018b). Novel P2-type Concentration-Gradient Na0.67Ni0.167Co0.167Mn0.67O2 Modified by Mn-Rich Surface as Cathode Material for Sodium Ion Batteries. *J. Power Sources* 396, 404–411. doi:10.1016/j.jpowsour.2018.06.050

Bao, S., Luo, S.-h., Wang, Z.-Y., Yan, S.-X., and Wang, Q. (2018a). Novel High-Capacity Hybrid Layered Oxides NaxLi1.5-xNi0.167Co0.167Mn0.67O2 as Promising Cathode Materials for Rechargeable Sodium Ion Batteries. *Ceram. Int.* 44, 22512–22519. doi:10.1016/j.ceramint.2018.09.022

Bao, S., Luo, S., Wang, Z., Wang, Q., Hao, A., Zhang, Y., et al. (2017). The Critical Role of Sodium Content on Structure, Morphology and Electrochemical Performance of Layered P2-type Na X Ni 0.167 Co 0.167 Mn 0.67 O 2 for Sodium Ion Batteries. *J. Power Sources* 362, 323–331. doi:10.1016/j.jpowsour.2017.07.057

Bauer, A., Song, J., Vail, S., Pan, W., Barker, J., and Lu, Y. (2018). The Scale-up and Commercialization of Nonaqueous Na-Ion Battery Technologies. *Adv. Energy Mat.* 8, 1702869. doi:10.1002/aenm.201702869

Bianchini, M., Roca-Ayats, M., Hartmann, P., Brezesinski, T., and Janek, J. (2019). There and Back Again-The Journey of LiNiO 2 as a Cathode Active Material. *Angew. Chem. Int. Ed.* 58, 10434–10458. doi:10.1002/anie.201812472

Boer, L., Pescatori, A., and Stuermer, M. (2021). *Energy Transition Metals*. Berlin: International Monetary Fund. Discussion Papers 1976.

Boer, L. (2022). *Steigende Metallpreise als mögliches Hindernis der Energiewende: DIW Wochenbericht Nr.4/2022*. Berlin: DIW - Deutsches Institut für Wirtschaftsforschung.

Buzgar, N., and Ionut Apopei, A. (2009). The Raman Study of Carbonates. *Geologie* 55, 97–112.

Casas-Cabanas, M., Reynaud, M., Rikarte, J., Horbach, P., and Rodríguez-Carvajal, J. (2016). FAULTS: a Program for Refinement of Structures with Extended Defects. *J. Appl. Cryst.* 49, 2259–2269. doi:10.1107/S1600576716014473

Clément, R. J., Bruce, P. G., and Grey, C. P. (2015). Review-Manganese-Based P2-type Transition Metal Oxides as Sodium-Ion Battery Cathode Materials. *J. Electrochem. Soc.* 162, A2589–A2604. doi:10.1149/2.0201514jes

Dai, K., Mao, J., Zhuo, Z., Feng, Y., Mao, W., Ai, G., et al. (2020). Negligible Voltage Hysteresis with Strong Anionic Redox in Conventional Battery Electrode. *Nano Energy* 74, 104831. doi:10.1016/j.nanoen.2020.104831

Delmas, C., Fouassier, C., and Hagenmuller, P. (1980). Structural Classification and Properties of the Layered Oxides. *Phys. B+C* 99, 81–85. doi:10.1016/0378-4363(80)90214-4

Duffort, V., Talaie, E., Black, R., and Nazar, L. F. (2015). Uptake of CO2in Layered P2-Na0.67Mn0.5Fe0.5O2: Insertion of Carbonate Anions. *Chem. Mat.* 27, 2515–2524. doi:10.1021/acs.chemmater.5b00097

Dunn, B., Kamath, H., and Tarascon, J.-M. (2011). Electrical Energy Storage for the Grid: a Battery of Choices. *Science* 334, 928–935. doi:10.1126/science.1212741

Feitknecht, W., Brunner, P., and Oswaldw, H. R. (1962). Über den Einfluß der Feuchtigkeit auf die Oxydation von Manganhydroxid durch molekularen Sauerstoff. *Z. Anorg. Allg. Chem.* 316, 154–160. doi:10.1002/zaac.19623160307

Feng, J., Luo, S.-h., Dou, Y., Cong, J., Liu, X., Li, P., et al. (2022). Facile Design and Synthesis of Co-free Layered O3-type NaNi0.2Mn0.2Fe0.6O2 as Promising Cathode Material for Sodium-Ion Batteries. *J. Electroanal. Chem.* 914, 116301. doi:10.1016/j.jelechem.2022.116301

Ghosh, S. K. (2020). Diversity in the Family of Manganese Oxides at the Nanoscale: From Fundamentals to Applications. *ACS Omega* 5, 25493–25504. doi:10.1021/acsomega.0c03455

Goikolea, E., Palomares, V., Wang, S., Larramendi, I. R., Guo, X., Wang, G., et al. (2020). Na-Ion Batteries-Approaching Old and New Challenges. *Adv. Energy Mat.* 10, 2002055. doi:10.1002/aenm.202002055

Gonzalo, E., Zarrabeitia, M., Drewett, N. E., López del Amo, J. M., and Rojo, T. (2021). López del Amo, Juan Miguel, and Rojo, TSodium manganese-rich layered oxides: Potential candidates as positive electrode for Sodium-ion batteries. *Energy Storage Mater.* 34, 682–707. doi:10.1016/j.ensm.2020.10.010

Guo, L., Gu, W., Peng, C., Wang, W., Li, Y. J., Zong, T., et al. (2019). A Comprehensive Study of Hygroscopic Properties of Calcium- and Magnesium-Containing Salts: Implication for Hygroscopicity of Mineral Dust and Sea Salt Aerosols. *Atmos. Chem. Phys.* 19, 2115–2133. doi:10.5194/acp-19-2115-2019

Gupta, P., Pushpakanth, S., Haider, M. A., and Basu, S. (2022). Understanding the Design of Cathode Materials for Na-Ion Batteries. *ACS Omega* 7, 5605–5614. doi:10.1021/acsomega.1c05794

Gür, T. M. (2018). Review of Electrical Energy Storage Technologies, Materials and Systems: Challenges and Prospects for Large-Scale Grid Storage. *Energy Environ. Sci.* 11, 2696–2767. doi:10.1039/C8EE01419A

Gutierrez, A., Dose, W. M., Borkiewicz, O., Guo, F., Avdeev, M., Kim, S., et al. (2018). On Disrupting the Na+-Ion/Vacancy Ordering in P2-type Sodium-Manganese-Nickel Oxide Cathodes for Na+-Ion Batteries. *J. Phys. Chem. C* 122, 23251–23260. doi:10.1021/acs.jpcc.8b05537

Hasa, I., Buchholz, D., Passerini, S., and Hassoun, J. (2015). A Comparative Study of Layered Transition Metal Oxide Cathodes for Application in Sodium-Ion Battery. *ACS Appl. Mat. Interfaces* 7, 5206–5212. doi:10.1021/am5080437

Hasa, I., Buchholz, D., Passerini, S., Scrosati, B., and Hassoun, J. (2014). High Performance Na0.5[Ni0.23Fe0.13Mn0.63]O2Cathode for Sodium-Ion Batteries. *Adv. Energy Mat.* 4, 1400083. doi:10.1002/aenm.201400083

Hasa, I., Mariyappan, S., Saurel, D., Adelhelm, P., Koposov, A. Y., Masquelier, C., et al. (2021). Challenges of Today for Na-Based Batteries of the Future: From Materials to Cell Metrics. *J. Power Sources* 482, 228872. doi:10.1016/j.jpowsour.2020.228872

Hasa, I., Passerini, S., and Hassoun, J. (2017). Toward High Energy Density Cathode Materials for Sodium-Ion Batteries: Investigating the Beneficial Effect of Aluminum Doping on the P2-type Structure. *J. Mat. Chem. A* 5, 4467–4477. doi:10.1039/C6TA08667E

Huggins, R. A. (2009). *Advanced Batteries: Materials Science Aspects*. Boston, MA, US: Springer.

Iliev, M. N., Litvinchuk, A. P., Meng, R. L., Sun, Y. Y., Cmaidalka, J., and Chu, C. W. (2004). Raman Phonons and Ageing-Related Surface Disorder in NaxCoO2. *Phys. C. Supercond.* 402, 239–242. doi:10.1016/j.physc.2003.09.085

International Energy Agency (2021). *The Role of Critical Minerals in Clean Energy Transitions: World Energy Outlook Special Report*. Paris: IEA.

International Renewable Energy Agency (2021). *IRENA Renewable Energy Highlights*. Abu Dhabi: IRENA.

Jung, R., Strobl, P., Maglia, F., Stinner, C., and Gasteiger, H. A. (2018). Temperature Dependence of Oxygen Release from LiNi0.6Mn0.2Co0.2O2 (NMC622) Cathode Materials for Li-Ion Batteries. *J. Electrochem. Soc.* 165, A2869–A2879. doi:10.1149/2.1261811jes

Kubota, K., and Komaba, S. (2015). Review-Practical Issues and Future Perspective for Na-Ion Batteries. *J. Electrochem. Soc.* 162, A2538–A2550. doi:10.1149/2.0151514jes

Kubota, K., Kumakura, S., Yoda, Y., Kuroki, K., and Komaba, S. (2018). Electrochemistry and Solid-State Chemistry of NaMeO 2 (Me = 3d Transition Metals). *Adv. Energy Mat.* 8, 1703415. doi:10.1002/aenm.201703415

Kubota, K., Yoda, Y., and Komaba, S. (2017). Origin of Enhanced Capacity Retention of P2-type Na2/3Ni1/3-xMn2/3CuxO2for Na-Ion Batteries. *J. Electrochem. Soc.* 164, A2368–A2373. doi:10.1149/2.0311712jes

Kuze, S., Kageura, J.-i., Matsumoto, S., Nakayama, T., Makidera, M., Saka, M., et al. (2013). *Development of a Sodium Ion Secondary Battery*. Tokyo: R&D Report.

Larcher, D., and Tarascon, J.-M. (2015). Towards Greener and More Sustainable Batteries for Electrical Energy Storage. *Nat. Chem.* 7, 19–29. doi:10.1038/nchem.2085

Lee, D. H., Xu, J., and Meng, Y. S. (2013). An Advanced Cathode for Na-Ion Batteries with High Rate and Excellent Structural Stability. *Phys. Chem. Chem. Phys.* 15, 3304–3312. doi:10.1039/c2cp44467d

Lei, Y., Li, X., Liu, L., and Ceder, G. (2014). Synthesis and Stoichiometry of Different Layered Sodium Cobalt Oxides. *Chem. Mat.* 26, 5288–5296. doi:10.1021/cm5021788

Lemmens, P., Gnezdilov, V., Kovaleva, N. N., Choi, K. Y., Sakurai, H., Takayama-Muromachi, E., et al. (2004). Effect of Na Content and Hydration on the Excitation Spectrum of the Cobaltite NaxCoO2·yH2O. *J. Phys. Condens. Matter* 16, S857–S865. doi:10.1088/0953-8984/16/11/041

Liu, Y., Fang, X., Zhang, A., Shen, C., Liu, Q., Enaya, H. A., et al. (2016). Layered P2-Na2/3[Ni1/3Mn2/3]O2 as High-Voltage Cathode for Sodium-Ion Batteries: The Capacity Decay Mechanism and Al2O3 Surface Modification. *Nano Energy* 27, 27–34. doi:10.1016/j.nanoen.2016.06.026

Lu, Z., and Dahn, J. R. (2001a). *In Situ* X-Ray Diffraction Study of P2-Na[sub 2/3][Ni[sub 1/3]Mn[sub 2/3]]O[sub 2]. *J. Electrochem. Soc.* 148, A1225. doi:10.1149/1.1407247

Lu, Z., and Dahn, J. R. (2001b). Intercalation of Water in P2, T2 and O2 Structure Az[CoxNi1/3-xMn2/3]O2. *Chem. Mat.* 13, 1252–1257. doi:10.1021/cm000721x

Manikandan, P., Ramasubramonian, D., and Shaijumon, M. M. (2016). Layered P2-type Na0.5Ni0.25Mn0.75O2 as a High Performance Cathode Material for Sodium-Ion Batteries. *Electrochimica Acta* 206, 199–206. doi:10.1016/j.electacta.2016.04.138

Manthiram, A. (2017). An Outlook on Lithium Ion Battery Technology. *ACS Cent. Sci.* 3, 1063–1069. doi:10.1021/acscentsci.7b00288

Momma, K., and Izumi, F. (2011). VESTA 3for Three-Dimensional Visualization of Crystal, Volumetric and Morphology Data. *J. Appl. Cryst.* 44, 1272–1276. doi:10.1107/S0021889811038970

Ortiz-Vitoriano, N., Drewett, N. E., Gonzalo, E., and Rojo, T. (2017). High Performance Manganese-Based Layered Oxide Cathodes: Overcoming the Challenges of Sodium Ion Batteries. *Energy Environ. Sci.* 10, 1051–1074. doi:10.1039/C7EE00566K

Owen, B. (1965). Some Stability Relations in the System Mn-O2-H2o at 25° and One Atmosphere Total Pressure. *Am. Mineralogist* 50, 1296–1354.

Padhi, A. K., Nanjundaswamy, K. S., and Goodenough, J. B. (1997a). Phospho-olivines as Positive-Electrode Materials for Rechargeable Lithium Batteries. *J. Electrochem. Soc.* 144, 1188–1194. doi:10.1149/1.1837571

Padhi, A. K., Nanjundaswamy, K. S., Masquelier, C., Okada, S., and Goodenough, J. B. (1997b). Effect of Structure on the Fe3 + / Fe2 + Redox Couple in Iron Phosphates. *J. Electrochem. Soc.* 144, 1609–1613. doi:10.1149/1.1837649

Paulsen, J. M., and Dahn, J. R. (1999). Studies of the Layered Manganese Bronzes, Na2/3[Mn1−xMx]O2 with M=Co, Ni, Li, and Li2/3[Mn1−xMx]O2 Prepared by Ion-Exchange. *Solid State Ionics* 126, 3–24. doi:10.1016/S0167-2738(99)00147-2

Paulsen, J. M., Thomas, C. L., and Dahn, J. R. (1999). Layered Li-Mn-Oxide with the O2 Structure: A Cathode Material for Li-Ion Cells Which Does Not Convert to Spinel. *J. Electrochem. Soc.* 146, 3560–3565. doi:10.1149/1.1392514

Pritzl, D., Teufl, T., Freiberg, A. T. S., Strehle, B., Sicklinger, J., Sommer, H., et al. (2019). Editors' Choice-Washing of Nickel-Rich Cathode Materials for Lithium-Ion Batteries: Towards a Mechanistic Understanding. *J. Electrochem. Soc.* 166, A4056–A4066. doi:10.1149/2.1351915jes

Qu, J. F., Wang, W., Chen, Y., Li, G., and Li, X. G. (2006). Raman Spectra Study on Nonstoichiometric compoundNaxCoO2. *Phys. Rev. B* 73, 250. doi:10.1103/PhysRevB.73.092518

Risthaus, T., Chen, L., Wang, J., Li, J., Zhou, D., Zhang, L., et al. (2019). P3 Na0.9Ni0.5Mn0.5O2 Cathode Material for Sodium Ion Batteries. *Chem. Mat.* 31, 5376–5383. doi:10.1021/acs.chemmater.8b03270

Rudola, A., Rennie, A. J. R., Heap, R., Meysami, S. S., Lowbridge, A., Mazzali, F., et al. (2021). Commercialisation of High Energy Density Sodium-Ion Batteries: Faradion's Journey and Outlook. *J. Mat. Chem. A* 9, 8279–8302. doi:10.1039/D1TA00376C

Sathiya, M., Thomas, J., Batuk, D., Pimenta, V., Gopalan, R., and Tarascon, J.-M. (2017). Dual Stabilization and Sacrificial Effect of Na2CO3 for Increasing Capacities of Na-Ion Cells Based on P2-NaxMO2 Electrodes. *Chem. Mat.* 29, 5948–5956. doi:10.1021/acs.chemmater.7b01542

Schipper, F., Erickson, E. M., Erk, C., Shin, J.-Y., Chesneau, F. F., and Aurbach, D. (2017). Review-Recent Advances and Remaining Challenges for Lithium Ion Battery Cathodes. *J. Electrochem. Soc.* 164, A6220–A6228. doi:10.1149/2.0351701jes

Shkrob, I. A., Gilbert, J. A., Phillips, P. J., Klie, R., Haasch, R. T., Bareño, J., et al. (2017). Chemical Weathering of Layered Ni-Rich Oxide Electrode Materials: Evidence for Cation Exchange. *J. Electrochem. Soc.* 164, A1489–A1498. doi:10.1149/2.0861707jes

Sicklinger, J., Metzger, M., Beyer, H., Pritzl, D., and Gasteiger, H. A. (2019). Ambient Storage Derived Surface Contamination of NCM811 and NCM111: Performance Implications and Mitigation Strategies. *J. Electrochem. Soc.* 166, A2322–A2335. doi:10.1149/2.0011912jes

Singh, G., Galceran, M., Pérez-Villar, S., and Rojo, T. (2015). Structural Evolution during Sodium Deintercalation/intercalation in Na2/3[Fe1/2Mn1/2]O2Structural Evolution during Sodium Deintercalation/intercalation in Na 2/3 [Fe 1/2 Mn 1/2]O 2. *J. Mat. Chem. A* 3, 6954–6961. doi:10.1039/c4ta06360k

Singh, G., Tapia-Ruiz, N., Lopez del Amo, J. M., Maitra, U., Somerville, J. W., Armstrong, A. R., et al. (2016). High Voltage Mg-Doped Na0.67Ni0.3-xMgxMn0.7O2 (X = 0.05, 0.1) Na-Ion Cathodes with Enhanced Stability and Rate Capability. *Chem. Mat.* 28, 5087–5094. doi:10.1021/acs.chemmater.6b01935

Sun, Y.-K. (2020). Direction for Commercialization of O3-type Layered Cathodes for Sodium-Ion Batteries. *ACS Energy Lett.* 5, 1278–1280. doi:10.1021/acsenergylett.0c00597

Tapia-Ruiz, N., Armstrong, A. R., Alptekin, H., Amores, M. A., Au, H., Barker, J., et al. (2021). 2021 Roadmap for Sodium-Ion Batteries. *J. Phys. Energy* 3, 031503. doi:10.1088/2515-7655/ac01ef

Tapia-Ruiz, N., Dose, W. M., Sharma, N., Chen, H., Heath, J., Somerville, J. W., et al. (2018). High Voltage Structural Evolution and Enhanced Na-Ion Diffusion in P2-Na2/3Ni1/3−xMgxMn2/3O2 ($0 \leq X \leq 0.2$) Cathodes from Diffraction, Electrochemical and Ab Initio Studies. *Energy Environ. Sci.* 11, 1470–1479. doi:10.1039/C7EE02995K

Tarascon, J.-M. (2020). Na-ion versus Li-Ion Batteries: Complementarity rather Than Competitiveness. *Joule* 4, 1616–1620. doi:10.1016/j.joule.2020.06.003

Teichert, P., Eshetu, G. G., Jahnke, H., and Figgemeier, E. (2020). Degradation and Aging Routes of Ni-Rich Cathode Based Li-Ion Batteries. *Batteries* 6, 8. doi:10.3390/batteries6010008

UNFCCC (2022). *Report of the Conference of the Parties on its Twenty-Sixth Session, Held in Glasgow from 31 October to 12 November 2021: FCCC/CP/2021/12*. New York City, NY: Advance Version.

Vaalma, C., Buchholz, D., Weil, M., and Passerini, S. (2018). A Cost and Resource Analysis of Sodium-Ion Batteries. *Nat. Rev. Mater* 3, 1–11. doi:10.1038/natrevmats.2018.13

Wang, P.-F., You, Y., Yin, Y.-X., and Guo, Y.-G. (2018). Layered Oxide Cathodes for Sodium-Ion Batteries: Phase Transition, Air Stability, and Performance. *Adv. Energy Mat.* 8, 1701912. doi:10.1002/aenm.201701912

Wang, P.-F., You, Y., Yin, Y.-X., Wang, Y.-S., Wan, L.-J., Gu, L., et al. (2016). Suppressing the P2-O2 Phase Transition of Na0.67 Mn0.67 Ni0.33 O2 by Magnesium Substitution for Improved Sodium-Ion Batteries. *Angew. Chem. Int. Ed.* 55, 7445–7449. doi:10.1002/anie.201602202

Wu, X., Xu, G.-L., Zhong, G., Gong, Z., McDonald, M. J., Zheng, S., et al. (2016). Insights into the Effects of Zinc Doping on Structural Phase Transition of P2-type Sodium Nickel Manganese Oxide Cathodes for High-Energy Sodium Ion Batteries. *ACS Appl. Mat. Interfaces* 8, 22227–22237. doi:10.1021/acsami.6b06701

Xiao, B., Liu, X., Song, M., Yang, X., Omenya, F., Feng, S., et al. (2021). A General Strategy for Batch Development of High-Performance and Cost-Effective Sodium Layered Cathodes. *Nano Energy* 89, 106371. doi:10.1016/j.nanoen.2021.106371

Yabuuchi, N., Kajiyama, M., Iwatate, J., Nishikawa, H., Hitomi, S., Okuyama, R., et al. (2012). P2-type Nax[Fe1/2Mn1/2]O2 Made from Earth-Abundant Elements for Rechargeable Na Batteries. *Nat. Mater* 11, 512–517. doi:10.1038/nmat3309

Yang, H. X., Xia, Y., Shi, Y. G., Tian, H. F., Xiao, R. J., Liu, X., et al. (2006). Raman Spectroscopy Study of α -, β -, γ−NaxCoO2 and γ−(Ca,Sr)xCoO2. *Phys. Rev. B* 74, 424. doi:10.1103/PhysRevB.74.094301

Yang, L., Luo, S.-h., Wang, Y., Zhan, Y., Wang, Q., Zhang, Y., et al. (2021). Cu-doped Layered P2-type Na0.67Ni0.33-xCuxMn0.67O2 Cathode Electrode Material with Enhanced Electrochemical Performance for Sodium-Ion Batteries. *Chem. Eng. J.* 404, 126578. doi:10.1016/j.cej.2020.126578

Yoshida, H., Yabuuchi, N., Kubota, K., Ikeuchi, I., Garsuch, A., Schulz-Dobrick, M., et al. (2014). P2-type Na2/3Ni1/3Mn2/3−xTixO2 as a New Positive Electrode for Higher Energy Na-Ion Batteries. *Chem. Commun.* 50, 3677–3680. doi:10.1039/c3cc49856e

Zhang, S. S. (2014). Insight into the Gassing Problem of Li-Ion Battery. *Front. Energy Res.* 2, 8694. doi:10.3389/fenrg.2014.00059

Zhang, Y., Wu, M., Ma, J., Wei, G., Ling, Y., Zhang, R., et al. (2020). Revisiting the Na2/3Ni1/3Mn2/3O2 Cathode: Oxygen Redox Chemistry and Oxygen Release Suppression. *ACS Cent. Sci.* 6, 232–240. doi:10.1021/acscentsci.9b01166

Zhao, C., Wang, Q., Yao, Z., Wang, J., Sánchez-Lengeling, B., Ding, F., et al. (2020). Rational Design of Layered Oxide Materials for Sodium-Ion Batteries. *Science* 370, 708–711. doi:10.1126/science.aay9972

Zheng, L., Li, J., and Obrovac, M. N. (2017). Crystal Structures and Electrochemical Performance of Air-Stable Na2/3Ni1/3-xCuxMn2/3O2 in Sodium Cells. *Chem. Mat.* 29, 1623–1631. doi:10.1021/acs.chemmater.6b04769

Zuo, W., Qiu, J., Liu, X., Ren, F., Liu, H., He, H., et al. (2020). The Stability of P2-Layered Sodium Transition Metal Oxides in Ambient Atmospheres. *Nat. Commun.* 11, 3544. doi:10.1038/s41467-020-17290-6

Conflict of Interest: The authors declare that the research was conducted in the absence of any commercial or financial relationships that could be construed as a potential conflict of interest.

Publisher's Note: All claims expressed in this article are solely those of the authors and do not necessarily represent those of their affiliated organizations, or those of the publisher, the editors and the reviewers. Any product that may be evaluated in this article, or claim that may be made by its manufacturer, is not guaranteed or endorsed by the publisher.